A Dynamically Consistent Reconstruction of Ocean Temperature

SAMUEL S. P. SHEN

Department of Mathematics and Statistics, San Diego State University, San Diego, and Scripps Institution of Oceanography, University of California, San Diego, La Jolla, California

GREGORY P. BEHM

Department of Mathematics and Statistics, San Diego State University, San Diego, California

Y. TONY SONG

Jet Propulsion Laboratory, California Institute of Technology, Pasadena, California

TANGDONG QU

Joint Institute for Regional Earth System Science and Engineering, University of California, Los Angeles, Los Angeles, California

(Manuscript received 3 July 2016, in final form 4 February 2017)

ABSTRACT

This paper provides a spectral optimal gridding (SOG) method to make a dynamically consistent reconstruction of water temperature for the global ocean at different depth levels. The dynamical consistency is achieved by using the basis of empirical orthogonal functions (EOFs) derived from NASA Jet Propulsion Laboratory (JPL) non-Boussinesq ocean general circulation model (OGCM) output at $^1/_4°$ resolution from 1958 to 2013. A convenient singular value decomposition (SVD) method is used to calculate the EOFs, in order to enable efficient computing for a fine spatial grid globally. These EOFs are used as explainable variables and are regressed against the sparsely distributed in situ ocean temperature data at 33 standard depth levels. The observed data are aggregated onto a 1° latitude–longitude grid at each level from the surface to the 5500-m layer for the period 1950–2014. Three representative temperature reconstruction examples are presented and validated: two 10-m-layer (i.e., the second layer from the surface) reconstructions for January 2008 and January 1998, which are compared with independent sea surface temperature (SST) observations; and one 100-m-layer reconstruction for January 1998, which shows a strong cold anomaly El Niño signal in the western tropical Pacific up to −5°C from 150°E to 140°W. The SOG reconstruction can accurately locate the El Niño signal region in different ocean layers. The SOG reconstruction method is shown reliable and yields satisfactory accuracy even with sparse data. Validation and error analysis indicate that no systematic biases exist in the observed and reconstructed data.

1. Introduction

Gridding temperature at different levels of the global ocean is key to locating Earth's unbalanced heat intake from solar radiation, which is approximately 0.1–1.1 W m^{-2} (Llovel et al. 2014; Loeb et al. 2012; Trenberth and Fasullo 2009, 2010; Trenberth et al. 2009; Hansen et al. 2005, 2011). Many reconstructed products are available to quantify this imbalance and its uncertainty, to find the locations of the heat in specific layers of ocean, and to have other applications, such as sea level predictions and ocean model validations (e.g., Roemmich et al. 2015; Meehl et al. 2011; Levitus et al. 2005; Smith et al. 2008). Each product has its own merits, scientific features, and limitations. Because of the relative abundance of surface data, sea surface temperature (SST) reconstruction has been studied more often than the temperature of deeper layers. Various kinds of gridded SST products are available (Smith et al. 1996; Kaplan et al. 1998; Smith et al. 2008; Rayner et al. 2003). Recent studies have turned attention to deep oceans to explore the new frontiers in

Corresponding author e-mail: Samuel S. P. Shen, sam.shen@sdsu.edu

DOI: 10.1175/JTECH-D-16-0133.1

© 2017 American Meteorological Society. For information regarding reuse of this content and general copyright information, consult the AMS Copyright Policy (www.ametsoc.org/PUBSReuseLicenses).

Brought to you by NOAA Central Library | Unauthenticated | Downloaded 01/16/24 07:32 PM UTC

oceanic research but are mostly limited to the depth of 700 m, where many expendable bathythermograph (XBT) observations are available since the 1950s (Song and Colberg 2011; Murphy et al. 2009; Ishii and Kimoto 2009; Levitus et al. 2005; Lyman et al. 2010), and to 2000 m or deeper since the Argo data became available since the early 2000s (Gille 2002, 2008; Roemmich et al. 2012; Roemmich and Johnson 2012; von Schuckmann et al. 2014; Desbruyères et al. 2014; Levitus et al. 2012; Dunstone 2014; Abraham et al. 2013; Azaneu et al. 2013; Mauritzen et al. 2012). Data gridding at levels deeper than 2000 m has much uncertainty due to the scarcity of the observed data there (Cabanes et al. 2013; Gasparin et al. 2015; Balmaseda et al. 2013; Purkey and Johnson 2010). The objective analysis method has been widely used to grid the data of the second layer down to 700 m and has successfully detected a warming trend in the upper ocean (e.g., Levitus et al. 2005). However, objective analysis is not applicable to the deep ocean, where data coverage is extremely sparse and teleconnection properties must be utilized (Roemmich et al. 2015; Shen et al. 2004; Smith et al. 1998). Even in the upper-ocean reconstructions, a recent study shows that the observed estimates of 0–700-dbar (approximately equivalent to the top 700 m of the ocean layer) global ocean warming during 1970–2004 are likely too low, due to poor sampling of the Southern Hemisphere and the limitations of the analysis methods that conservatively estimate temperature changes in data-sparse regions (Durack et al. 2014). A need for making a very reliable reconstruction of the full-depth ocean based on the scarce in situ data is imminent.

The purpose of this paper is to present a spectral optimal gridding (SOG) method that can make dynamically consistent reconstruction of oceanic data applicable to regions with poor sampling, such as deep ocean levels and the Southern Oceans, and can also yield an error estimate for the reconstruction. Our method uses the non-Boussinesq ocean general circulation model (OGCM) output for building empirical orthogonal functions (EOFs) and regressing the EOFs against the sparsely distributed in situ observational data. The non-Boussinesq OGCM allows its solutions of sea level and ocean bottom pressure variations to be consistent with satellite altimetry and gravimetry data, respectively. Our multivariate analysis approach comes handily with an array of error estimates, ranging from the mean-square error (MSE), to confidence intervals of EOF coefficients. The mathematical framework also allows for optimal model selection using Akaike information criterion (AIC). Our reconstruction method and product thus have two distinct features: (i) dynamic consistency guaranteed by the use of the NASA Jet Propulsion Laboratory (JPL) non-Boussinesq OGCM (Song and Hou 2006; Song et al. 2010) and (ii) use of the latest bias-corrected oceanic in situ data.

The dynamic consistency is critically important in gridding data-sparse regions. Meehl et al. (2011) found evidence of heat transport to deep ocean through the deep and bottom water formation at high latitudes during decades of slow warming. Different from the reconstructed SST data, the deep ocean reconstructed temperature data are very sensitive to the dynamical consistency, since the water mass expansion due to heat intake is nonnegligible. Song and Colberg (2011) and Llovel et al. (2014) quantified the dynamical consistency of sea level, ocean mass, upper-ocean steric expansion (0–700 m), and deep ocean expansion (deeper than 700 m). This dynamical consistency is governed by a mass conservation equation through a sea level closure equation [see Eq. (5) of Song and Colberg 2011; Moon and Song 2013; Leuliette and Miller 2009; Leuliette 2011; Milne et al. 2009; Wunsch and Heimbach 2013]. Huang and Jin (2002) identified the existence of inconsistency between the Boussineq approximation and either altimetry sea surface height (SSH) or ocean bottom pressure (OBP) from the Gravity Recovery and Climate Experiment (GRACE). Song et al. (2010) remediated the inconsistency by introducing a non-Boussinesq approximation in the NASA JPL OGCM. Moon et al. (2013) validated the consistency of the model SSH by 25 years of satellite altimetry data and also the consistency of OBP by 15 years of gravimetry data. Our current paper introduces a multivariate reconstruction method to make dynamically consistent reconstruction of different levels of water temperature in the global ocean. The dynamical consistency is achieved by our use of the EOF basis derived from NASA JPL OGCM's monthly output with a spatial resolution of $1/4° \times 1/4°$ latitude–longitude. EOFs are used as explainable variables and are regressed against the sparsely distributed in situ water temperature observations. This method has been applied to all 33 standard depth layers up to 5500-m depth. We select three examples to describe our SOG temperature reconstruction procedures: January 2008 and January 1998 at the 10-m layer and January 1998 at the 100-m layer. These examples can be easily validated from known datasets, such as the NOAA National Centers for Environmental Prediction (NCEP)'s Global Ocean Data Assimilation System (GODAS) (http://www.cpc.ncep.noaa.gov/products/GODAS), and the University of Maryland's Simple Ocean Data Assimilation (SODA) ocean/sea ice reanalysis (http://www.atmos.umd.edu/~ocean/; Carton and Giese 2008), and NOAA Extended Reconstructed Sea Surface Temperature (ERSST) data (Huang et al. 2015).

The remainder of the paper is arranged as follows: Section 2 describes datasets and the EOF multivariate

Brought to you by NOAA Central Library | Unauthenticated | Downloaded 01/16/24 07:32 PM UTC

regression method, section 3 includes results and their validation, and section 4 contains conclusions and discussion.

2. Datasets and dynamically consistent reconstruction method

a. *Overall ideas of the dynamically consistent SOG method*

A key criterion for a successful climate reconstruction is that the reconstructed fields are dynamically consistent so that the conservation laws of energy, momentum, and mass still hold with the reconstructed data. Another criterion is the accurate quantification with minimum reconstructed errors even in the case of very sparse space–time observations for a complex field with teleconnections, which means that the field is correlated not only to its nearby points but also to points at a very large distance. Ocean data reconstruction, either temperature or salinity, needs to meet these two criteria and to overcome the two problems of 1) data scarcity in the deep ocean and 2) density inversion and instability of non-model-guided reconstructions. Our SOG method can meet these criteria and differs from optimum interpolation (OI) and data assimilation approaches in the following three aspects:

(i) By taking into account the teleconnections and the ocean circulation patterns identified in the established OGCMs, the SOG approach can still make good reconstruction with sparse measurements, the commonly known situations in the deep and Southern Oceans. The kriging-based OI statistics—that is, the semivariogram—has little content on dynamical properties, which is the source of dynamical inconsistency. The SOG covariance functions are a natural summation of eigenvalues and EOFs computed from dynamical ocean models output using the SVD orthonormal space–time decomposition (Cline and Dhillon 2006).

(ii) The SOG approach relies on dynamically consistent data statistics for spatial structures, such as El Niño, and is still a statistical analysis of the data, while the data assimilation approach relies on the dynamical constraint penalized by differences between the model output and incomplete observational data. SOG results are a model-guided data output, while the data assimilation results are a data-constrained model output. Thus, SOG reconstruction is not affected by the model bias or drift because only the circulation patterns are used.

(iii) The SOG approach via multivariate regression can utilize a suite of advanced statistical tools of error estimation. Statistical inferences can also be made based on the regression results and their errors (Johnson and Wichern 2007). Comparatively, the kriging-based OI approach does not yield reliable errors, while the data assimilation approach has difficulties providing error estimates due to the complexity of nonlinearity and chaotic characteristics in a thermodynamic oceanic or atmospheric system.

Specifically, our SOG procedure is to expand the temperature at an ocean layer into EOFs calculated from the JPL OGCM, where the expansion coefficients are determined using the observational data through a multivariate regression theory. Therefore, our SOG approach needs both the OGCM output to determine the EOFs and the in situ data to determine the regression coefficients. In that sense, the ocean model provides the dynamically consistent circulation patterns in the gridding process, while the observed in situ data determine the variation magnitudes and trends of the final products of gridding.

b. *Data*

This subsection describes the details of the aforementioned two datasets used in our SOG method: the JPL OGCM output (Song and Hou 2006; Song et al. 2010) for EOF calculation and covariance modeling, and the in situ temperature data in the World Ocean Database 2009 (Locarnini et al. 2010; Zhang and Qu 2015) aggregated on grid boxes, which are for computing the multivariate regression coefficients.

1) NASA JPL OGCM OUTPUT

The non-Boussinesq NASA JPL OGCM used here was developed to better simulate satellite observations, such as altimetry SSH and GRACE's ocean bottom pressure (Song and Hou 2006; Song and Colberg 2011). The non-Boussinesq model's mass-conserving feature can help quantify the sea level rise due to thermosteric expansion of ocean warming. Thus, the model has successfully simulated the sea level rise as a direct response to the heat added into the ocean while maintaining the mass-conserving feature consistent with GRACE data (Song and Colberg 2011; Moon et al. 2013; Chen et al. 2014; Gregory and Lowe 2000; Greatbatch 1994; Griffies and Greatbatch 2012). This critical feature of the NASA JPL OGCM allows us to use the model output to build EOFs for our SOG reconstruction of the ocean temperature data up to 5500 m depth.

The current state-of-the-art free-surface NASA JPL OGCM is based on the Regional Ocean Modeling System (ROMS), which is a primitive equation ocean circulation model developed at the University of California, Los Angeles (UCLA), and Rutgers, The State University of

Brought to you by NOAA Central Library | Unauthenticated | Downloaded 01/16/24 07:32 PM UTC

New Jersey (Shchepetkin and McWilliams 2005, Haidvogel et al. 2008). The ROMS has the advantage of terrain following, which allows more flexibility in choosing vertical levels in specific vertical domains, such as the bottom boundary layer or surface mixed layer, and hence it yields better numerical accuracy of mass conservation in the model runs (Song and Haidvogel 1994) compared with the traditional sigma-coordinate system. The accuracy of mass conservation is critical in quantifying the sea level rise due to heat and freshwater input into the ocean. The non-Boussinesq ROMS includes a coupled sea ice model and has incorporated freshwater fluxes based on the Greenland and Antarctica ice melting data by Bamber et al. (2012). The model's North Pole is shifted to continental Russia to avoid the computational singularity. Horizontal resolution is ¼°. The model incorporates global digital elevation model (ETOPO2) topography, with modification from the U.S. Navy's Digital Bathymetry Data Base with 2-min resolution (DBDB2) bathymetry to accommodate complex geometry in the vicinities of straits. To initialize an approximate steady state, the model is spun up for 60 years with annual climatology forcing and then driven by daily NCEP–NCAR reanalysis forcing from 1948 to 2013. The 1948–57 OGCM output is dropped to reduce the influence of initial conditions.

Ocean surface heat flux is constrained by the value of net top-of-atmosphere (TOA) energy imbalance, which is $0.9 \pm 0.5\,\mathrm{W\,m^{-2}}$ in our model (Trenberth and Fasullo 2010). This is consistent with the observed increasing concentrations of carbon dioxide and other greenhouse gases that led to an imbalance at the top of the atmosphere of heat fluxes. The heat flux value used in our model is in the same order of $0.85 \pm 0.15\,\mathrm{W\,m^{-2}}$ used by Hansen et al. (2005), and $0.50 \pm 0.43\,\mathrm{W\,m^{-2}}$ from 2001 to 2010 estimated by Loeb et al. (2012). We understand that this heat flux value has large uncertainties (Johnson et al. 2016).

The model's space–time grid is as following. The model output is interpolated vertically into the standard 33 depth layers defined in Table 1. The horizontal resolution is ¼° latitude × ¼° longitude. The monthly model output is used. The space coverage is the entire global ocean. The time coverage is from January 1958 to December 2013. To match the in situ observations, the ¼° data are aggregated to a 1° grid by simple arithmetic average of the data on the sixteen ¼° boxes within a 1° box. The 1° data are then rearranged into a two-dimensional matrix, with N rows indexing the locations of N grid boxes and Y columns indexing the time of Y months. The entire OGCM output is an $N \times Y$ matrix. Here, N is the same as that in Table 1, the total number of boxes for a given layer. Note that N is 38 762 in the top layer and 38 770 for the second layer. The eight fewer boxes in the top layer are due to the OGCM's curvelinear coordinate design and the conversion from ¼° to 1° box (Song and Hou 2006). Another note is $N = 0$ for the 33rd layer at the 5500-m level, which is also due to the OGCM's coordinate system.

The SVD method is used to find the eigenvalues and eigenvectors of the covariance matrix built from this model output matrix.

2) In situ data

The in situ data used for the present study are from NOAA's National Oceanographic Data Center (NODC) (http://www.nodc.noaa.gov/OC5), including all individual temperature profiles at observed levels archived in the conductivity–temperature–depth (CTD), profiling float (PFL), and ocean station data (OSD) categories of the World Ocean Database 2009 (WOD09). Argo floating profiles are archived in the PFL category. Profiles collected after the release of WOD09 were also downloaded from the NODC website. We used the profile data only down to the depth of the 5500-m layer.

The original NODC profiles contain erroneous records in both coordinates and measured values, despite NODC's extensive editing and correction procedures. The NODC data were further scrutinized and only the profiles flagged with 0 (standing for "accepted") or 1 (for "possibly good") were taken (Qu et al. 1999; Zhang and Qu 2015; Qu et al. 2016). Some samples with missing values but mistakenly flagged with 0 were removed. If a profile has fewer than five samples, then it is most likely not reliable and hence removed. The samples at observed depths were converted onto the standard depth layers shown in Table 1. For each standard layer, both annual and seasonal standard deviation tests were applied on a 2° × 2° grid. Samples with a bias larger than three standard deviations were excluded. After these steps, 2 873 985 "reliable" casts over the global ocean are used for our SOG system. Figure 1a shows that for much of the global ocean, the number of reliable profiles in each 2° × 2° grid box of all layers is larger than 100 and exceeds 200 in some areas (e.g., the Kuroshio Extension and Gulf Stream region). The data coverage in the Southern Ocean is relatively poor, which is particularly so over the Antarctic Circumpolar Current region, where the number of samples in each 2° × 2° grid falls below 50 or less. The data spanned from 1950 to 2014 and had dense sampling during the periods of Tropical Ocean and Global Atmosphere (TOGA; 1985–95), the World Ocean Circulation Experiment (WOCE)'s field phase (1990–98), and Argo (2000–present) (Fig. 1b). Most of the observations are confined to the upper ocean, and the number of samples decreases rapidly with depth, falling below 200 000 at 2000 m in the deeper

Brought to you by NOAA Central Library | Unauthenticated | Downloaded 01/16/24 07:32 PM UTC

TABLE 1. Standard 33 ocean layers from the surface layer to the layer of 5500 m deep and their corresponding total number of 1° grid boxes and the number of grid boxes with data.

Layer No.	Depth level (m)	No. of grid boxes (N)	No. of climatology grid boxes	No. of data boxes (N_d) Jan 1998
1	0	38 762	18 980	152
2	10	38 770	34 632	928
3	20	38 614	34 672	916
4	30	38 216	34 668	916
5	50	37 883	34 472	888
6	75	37 594	34 164	848
7	100	37 124	33 856	796
8	125	36 766	33 708	764
9	150	36 463	33 580	728
10	200	36 167	33 360	692
11	250	35 689	33 188	672
12	300	35 249	32 928	656
13	400	34 909	32 540	616
14	500	34 431	32 200	600
15	600	34 009	31 708	548
16	700	33 686	31 472	512
17	800	33 394	31 276	504
18	900	33 130	31 136	480
19	1000	32 881	30 256	452
20	1100	32 638	29 612	408
21	1200	32 385	28 552	392
22	1300	32 137	28 200	376
23	1400	31 892	27 988	308
24	1500	31 652	27 128	232
25	1750	31 397	25 984	204
26	2000	30 757	9384	184
27	2500	30 087	6500	152
28	3000	25 526	5628	132
29	3500	20 737	4600	108
30	4000	14 831	3540	88
31	4500	8693	2396	64
32	5000	2627	1260	36
33	5500	0	356	16

layers (Fig. 2). The January climatology of a 2° × 2° grid box for a specific layer is defined as the space–time average of all the observed January data in the grid box from 1950 to 2014. At least two data records per space–time box are required for the monthly climatology calculation. The same computing procedure is used to calculate the grid box's climatology for other months (February, March, . . . , December) and for all the 2° × 2° grid boxes of every layer. Requiring more data points can improve the reliability of the climatology and anomaly results. However, for our given dataset, requiring more than two measurements dramatically decreases the number of available gridded anomalies for reconstruction, and hence results in less consistent reconstructions. Our monthly reconstructions from 1950 to 2014 at 2° × 2° resolution for the top 33 layers are made for anomalies with respect to this climatology. Nonetheless, more work needs to be done to understand the dataset, to improve the climatology calculation, and to produce anomalies for almost all the data.

The temperature climatology at the 10-m layer (i.e., the second layer in Table 1) is presented in Fig. 3 and shows essentially the same pattern as the *World Ocean Atlas 2013 Figures*, version 2 (*WOA13F V2*; Mishonov et al. 2013). Most basin-scale structures of circulation and water mass properties are well captured by this climatology.

To take advantage of the OGCM's high spatial resolution, we distribute the 2° × 2° data to 1° × 1° data by assigning the four 1° boxes the same data as the 2° data. Table 1 shows the number of data boxes for each layer N_d for January 1998. The total number of N_d data boxes for all layers and all months is 1 009 096, in contrast to the total number of profiles, 2 873 985. On average, every three profiles produce a 1° datum. Note that $N_d = 928$ for the second layer at the 10-m level is the maximum number of observations among the 33 layers and is larger than the top layer $N_d = 152$, because our dataset does not count for SST observations and most Argo floats do not take measurements in the top 5 m to avoid damaging float sensors (Anderson and Riser 2014).

Brought to you by NOAA Central Library | Unauthenticated | Downloaded 01/16/24 07:32 PM UTC

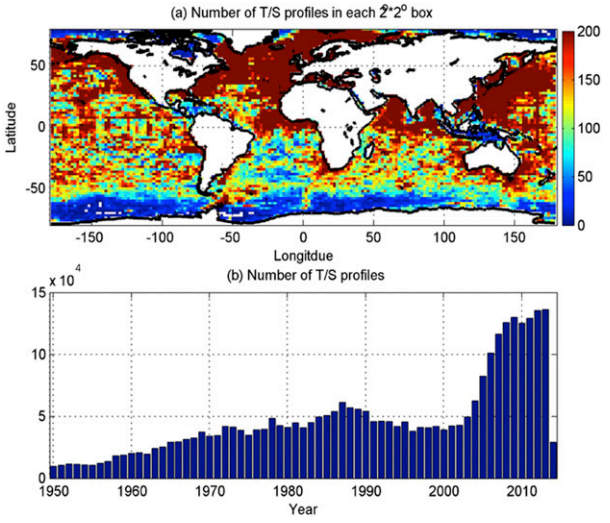

FIG. 1. (a) Density of observations: Number of profiles in each $2° \times 2°$ grid box for the entire period 1950–2014 for the top 33 layers from the surface layer to the 5500-m layer. (b) History of the number of profiles each year over the entire global ocean.

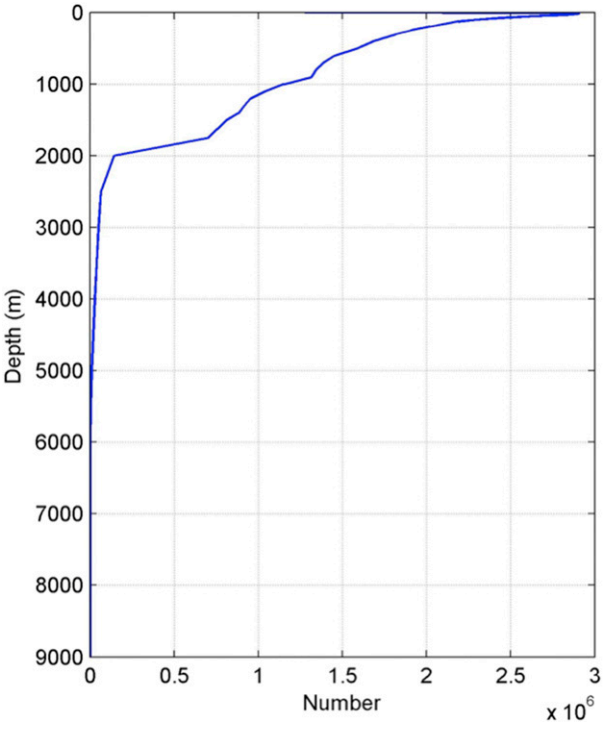

FIG. 2. Number of profile samplings as a function of depth over the global ocean and for the entire period 1950–2014.

Finally, our dynamically consistent SOG reconstruction uses the two datasets (OGCM output and the in situ observations) to produce a monthly $1° \times 1°$ reconstruction dataset from January 1950 to December 2014 for 32 layers from the second layer to the 33rd layer at 5500-m depth. The top layer—that is, the 0-m layer—is excluded because it does not have a corresponding OGCM output.

c. *The SOG reconstruction method*

Our dynamically consistent SOG reconstruction method is based on the theory of multivariate analysis (Johnson and Wichern 2007; Rawlings et al. 2001). Shen et al. (2014) described the SOG method for the global precipitation reconstruction. The SOG reconstruction part was essentially a multivariate version of the method of Smith et al. (2008) and Shen et al. (2004): minimizing MSE. This subsection recapitulates part of the theory already described in Shen et al. (2014) and provides additional specifics for the special needs of ocean data reconstruction.

The multivariate reconstruction model for the space–time ocean temperature field at grid box x and month t is

$$T(x,t) = \sum_{m\in\mathcal{M}} \beta_m(t)E_m(x)\Big/\sqrt{a(x)} + e(x,t). \qquad (1)$$

Here, $\beta_m(t)$ is the regression coefficient for the mth EOF $E_m(x)$; the least squares estimator of $\beta_m(t)$ is denoted by $b_m(t)$; $a(x) = \cos(\phi_x)$ is the area weight; ϕ_x is the centroid's latitude of x; $e(x, t)$ is the regression error whose variance is

$$\varepsilon^2(x,t) = \langle e^2(x,t)\rangle, \qquad (2)$$

which is to be estimated; and $\langle\cdot\rangle$ denotes the mathematical operation of expected value. The explanatory variable in the abovementioned multivariate regression is $E_m(x)$, computed from the area-weighted covariance matrix of the JPL OGCM output from the climatology period 1981–2010. Term $\mathcal{M}$ is the set of EOFs selected for our regression reconstruction. It is usually the first 20 EOFs or the M EOFs that account for 80% of the total variance, or it is determined by response data via a correlation test (Smith et al. 1998). The current paper uses the first 20 EOFs, when more than 20 observational data boxes are available, that is, $N_d > 20$. For deep ocean, M is smaller and is equal to N_d.

The EOFs are defined in the following way. The OGCM output's temperature anomaly data matrix is denoted by $\mathbf{T}^{\text{mod}}(x, t)$. For a given depth layer and a given month, $\mathbf{T}^{\text{mod}}(x, t)$ is a $N \times Y$ tall matrix, where N denotes the number of grid boxes at the given layer and Y is the temporal length of the model simulation, or another period, such as the climatology period from 1981 to 2010. Each datum is weighted by an area factor

$$\mathbf{T}^{\text{mod}}_{\text{area}}(x,t) = \mathbf{T}^{\text{mod}}(x,t)\sqrt{\cos(\phi_x)}. \qquad (3)$$

The area factor $\sqrt{\cos(\phi_x)}$ discounts the importance of the $1° \times 1°$ data over the polar regions compared with

Brought to you by NOAA Central Library | Unauthenticated | Downloaded 01/16/24 07:32 PM UTC

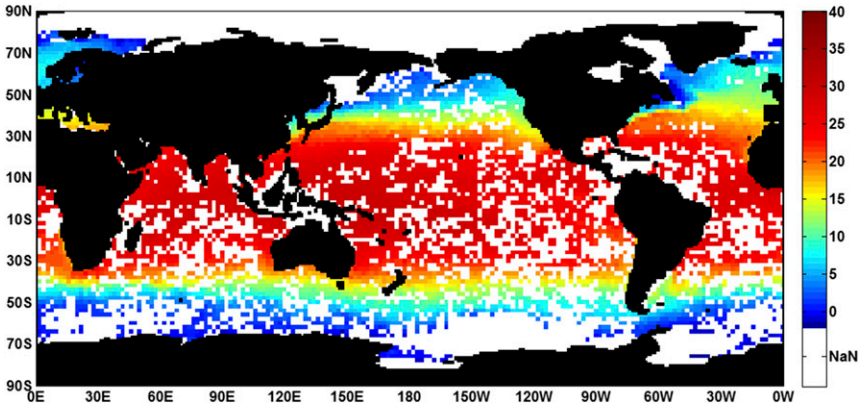

FIG. 3. The January climatology is calculated for each grid box when it has more than two entries during 1950–2014. It is a simple arithmetic mean of all the data in a box. If a box has only two or fewer readings, then the box is considered data void. This climatology may not be reliable for some individual grid boxes with only a few observations. The ones with a very large gradient with respect to its neighbors are considered suspicious and have been removed from this climatology map.

the equatorial regions. The covariance matrix for the model data is

$$\mathbf{C}(x,y) = \frac{1}{Y}[\mathbf{T}^{\text{mod}}_{\text{area}}(x,t)][\mathbf{T}^{\text{mod}}_{\text{area}}(y,t)]^{\text{T}}, \tag{4}$$

where $[\mathbf{T}^{\text{mod}}_{\text{area}}(y,t)]^{\text{T}}$ is the transpose of the matrix $[\mathbf{T}^{\text{mod}}_{\text{area}}(x,t)]$. Thus, $\mathbf{C}(x,y)$ is an $N \times N$ matrix with $N \gg Y$, whose eigenvalues and normalized eigenvectors are denoted by

$$[\lambda_m, E_m(x)] \quad m = 1,2,3,\ldots,Y \tag{5}$$

with

$$\sum_{x=1}^{N} [E_m(x)]^2 = 1. \tag{6}$$

The physical EOF on the spherical earth is weighted inversely by an area factor,

$$\psi_m(x) = E_m(x)/\sqrt{\cos(\phi_x)}. \tag{7}$$

This is an eigenfunction of the integral operator, whose kernel is the continuous temperature covariance function,

$$\int_{\Omega} T(x,t)T(y,t)\psi_m(y)\,dA_y = \lambda_m\psi_m(x), \quad m = 1,2,3,\ldots, \tag{8}$$

where Ω is the specific ocean layer region, dA_y is the differential area of the surface integral, and the eigenfunction normalization is

$$\int_{\text{layer}} [\psi_m(x)]^2\,dA_x = \left(\frac{\pi}{180}R\right)^2, \tag{9}$$

where R is Earth's radius. The continuous normalization [Eq. (9)] is equivalent to the discrete normalization [Eq. (6)] when neglecting the discretization error (Shen et al. 1998).

The observed monthly ocean temperature anomaly data are on scattered $1° \times 1°$ grid boxes, whose collection is the data domain Ω_d, a small subset of Ω. The data domain varies with time, since the number of ocean data profiles changes, in general increasing with time (see Fig. 1b). The orders of Ω, Ω_d and $\mathcal{M}$ sets are denoted by

$$\|\Omega\| = N, \quad \|\Omega_d\| = N_d, \quad \|\mathcal{M}\| = M. \tag{10}$$

The values of N and N_d are shown in Table 1 for each layer. As discussed earlier, M is usually set to be 20 in this paper, similar to that of Shen et al. (2014), which accounts for about 70%–80% of the total variance for the top few layers (see Figs. 4a and 4b). The observed data are denoted by

$$D(x,t), \quad x \in \Omega_d. \tag{11}$$

The sum of squared errors (SSE) over the spherical geometry is

$$\text{SSE} = \sum_{x\in\Omega_d} [D(x,t) - \hat{T}(x,t)]^2 a(x), \tag{12}$$

where

Brought to you by NOAA Central Library | Unauthenticated | Downloaded 01/16/24 07:32 PM UTC

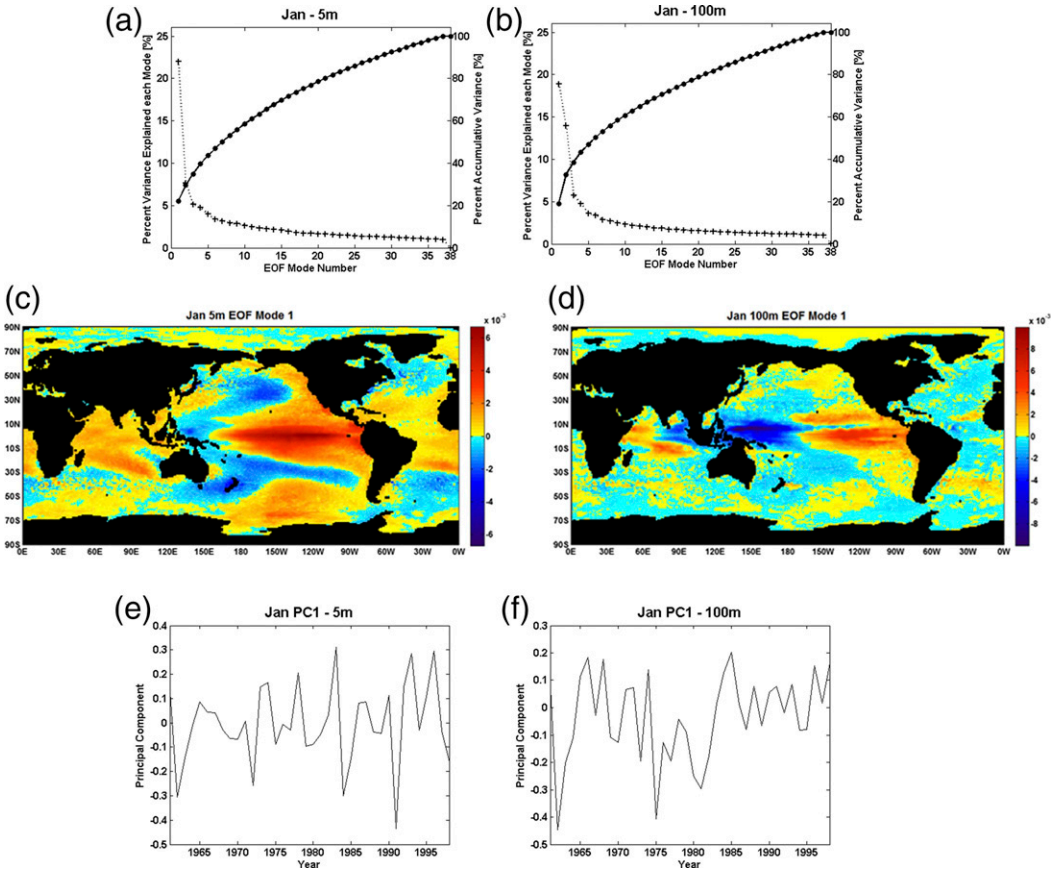

FIG. 4. (a) The January eigenvalues as the percentage of the total variance (the decreasing line marked by +) and their accumulations (the increasing line marked by solid dots) for the 5-m layer, indicated by 5 m in the JPL OGCM. The total variance is equal to the sum of all the eigenvalues. (b) As in (a), but for the 100 m-layer. (c) EOF1 for the 5-m layer, (d) EOF1 for the 100-m layer, (e) PC1 for the 5-m layer, (f) PC1 for the 100-m layer, (g) EOF2 for the 5-m layer, (h) EOF2 for the 100-m layer, (i) PC2 for the 5-m layer, (j) PC2 for the 100-m layer, (k) EOF3 for the 5-m layer, (l) EOF3 for the 100-m layer, (m) PC3 for the 5-m layer, and (n) PC3 for the 100-m layer.

$$\hat{T}(x,t) = \sum_{m\in\mathcal{M}} b_m(t)E_m(x)/\sqrt{a(x)} \tag{13}$$

is the temperature reconstruction, an estimate of the temperature field from the in situ data assisted by the JPL OGCM.

The SSE formula can be rewritten into

$$\mathrm{SSE} = \sum_{x\in\Omega_d} [D(x,t)\sqrt{a(x)} - \hat{T}(x,t)\sqrt{a(x)}]^2. \tag{14}$$

This is the standard least squares formulation in multivariate analysis for the area-weighted data $D(x, t)\sqrt{a(x)}$ (Johnson and Wichern 2007). The standard multivariate regression formulas can be applied to derive the reconstruction formula below:

$$[\hat{T}(x,t)\sqrt{a(x)}\,]_{N\times 1} = [E_m(x)]_{N\times M}\{[E_m(x_d)]^{\mathrm{T}}_{M\times N_d}[E_m(x_d)]_{N_d\times M}\}^{-1}[E_m(x_d)]^{\mathrm{T}}_{M\times N_d}[D(x,t)\sqrt{a(x)}\,]_{N_d\times 1} \tag{15}$$

This estimate's error variance with the area factor can be estimated by standard multivariate regression theory (Johnson and Wichern 2007),

$$\hat{\sigma}_a^2 = \frac{\mathrm{SSE}}{N_d - M - 1}. \tag{16}$$

The error variance for temperature without area factor is

$$\hat{\sigma}^2 = \frac{\|\hat{\boldsymbol{\varepsilon}}_{\boldsymbol{d}}\|^2}{N_d - M - 1}, \tag{17}$$

where the temperature residual vector without area factor is an $N_d \times 1$ vector $\hat{\boldsymbol{\varepsilon}}_d(x_d, t)$ defined by

$$\hat{\boldsymbol{\varepsilon}}_d(x_d,t) = [D(x_d,t) - \hat{\mathbf{T}}(x_d,t)]_{N_d\times 1} \tag{18}$$

Brought to you by NOAA Central Library | Unauthenticated | Downloaded 01/16/24 07:32 PM UTC

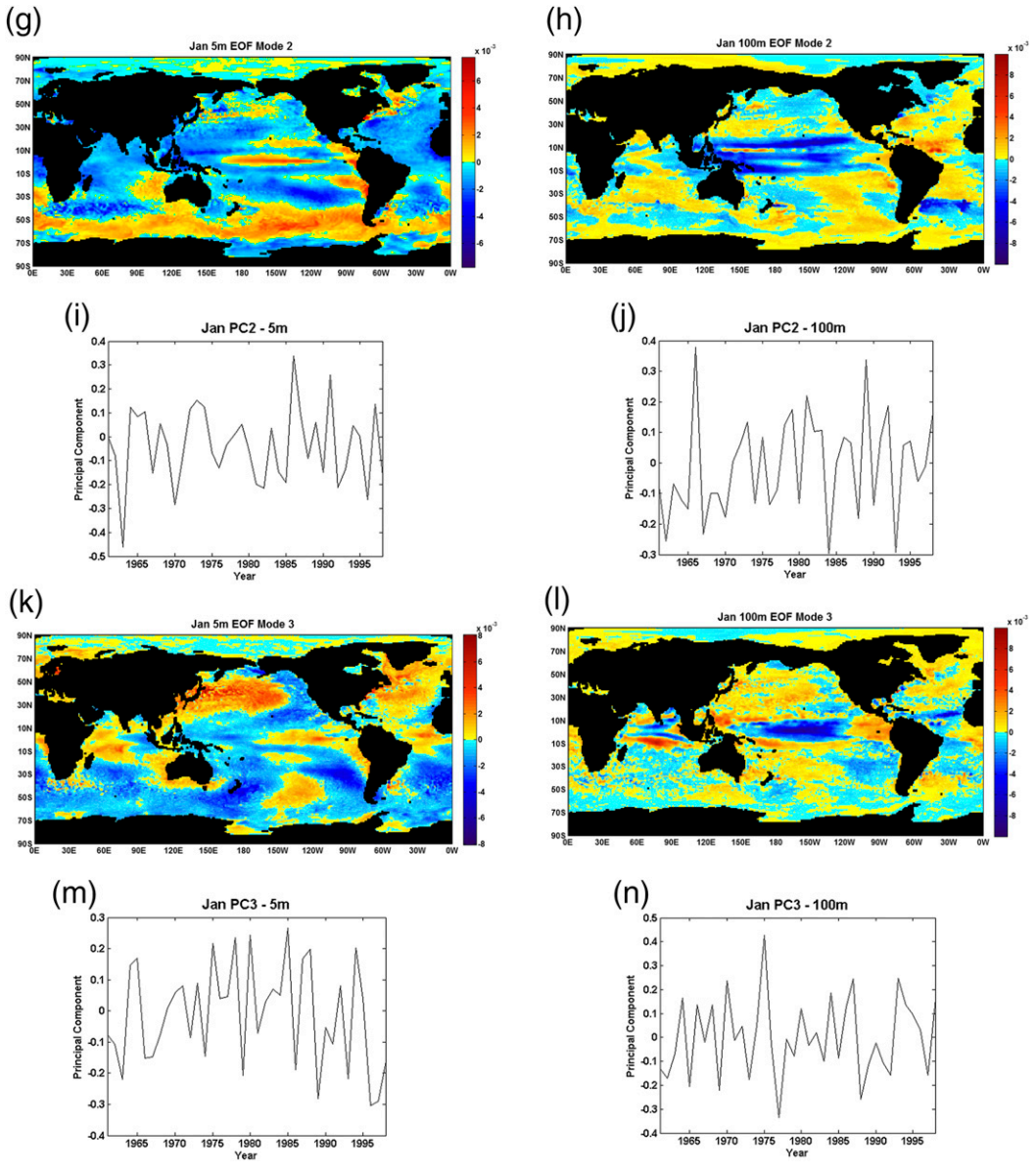

FIG. 4. (*Continued*)

and $\|\hat{\boldsymbol{\varepsilon}}_d\|^2$ is the regular Euclidean norm defined by

$$\|\hat{\boldsymbol{\varepsilon}}_d\|^2 = \sum_{x\in\Omega_d} [\widehat{\varepsilon}_d(x)]^2. \tag{19}$$

After obtaining the EOF matrix $[\mathbf{E}_m(x)]_{N\times 30}$, the reconstructed field can be easily obtained by matrix algebra of (15).

d. SVD approach to EOF calculations

While the multivariate regression method used in this paper is similar to that of Shen et al. (2014), the EOF calculation used a different approach. Shen et al. (2014) showed that the eigenvalue problem of the $N \times N$ spatial covariance matrix built from the $N \times 30$ (where $N \gg 30$) data matrix $[\mathbf{T}^{\text{mod}}_{\text{area}}(x, t)]$ could be efficiently computed from an equivalent 30×30 temporal covariance matrix. This space–time exchange reduced the EOF computing from solving an eigenvalue problem of a large spatial covariance matrix of order N—say, $N = 45\,000$—to solving an eigenvalue problem of a temporal covariance matrix of order 30. This greatly improved the computational efficiency and accuracy of EOFs and their eigenvalues. The large space dimension N in three-dimensional ocean data analysis requires even more efficient EOF computing algorithms that save the input/out process. When the ocean

Brought to you by NOAA Central Library | Unauthenticated | Downloaded 01/16/24 07:32 PM UTC

is divided into 33 layers at 1° resolution, N is in the order of one million. In this paper we use the singular value decomposition (SVD) approach to compute the eigenvalues and EOFs of the covariance matrix, while the covariance matrix does not need to be actually computed (Cline and Dhillon 2006). Skipping the step of explicit computation of the covariance matrix saves much input/output (I/O) time in computing.

In this paper, the SVD of the data matrix $[\mathbf{T}^{\text{mod}}_{\text{area}}(x, t)]$ is efficiently computed using Householder transforms (Cline and Dhillon 2006; Demmel and Kahan 1990). SVD, executed by simple R or MATLAB command svd($[\mathbf{T}^{\text{mod}}_{\text{area}}(x, t)]$), decomposes space–time data $[\mathbf{T}^{\text{mod}}_{\text{area}}(x, t)]_{N\times Y}$ of N grid boxes and Y time months into a space matrix $\mathbf{U}$ of EOFs and a time matrix $\mathbf{V}$ of principal components (PC), connected by an eigenvalue matrix $\mathbf{D}$ (or called energy matrix),

$$[\mathbf{T}^{\text{mod}}_{\text{area}}(x, t)] = \mathbf{UDV}^{\text{T}}. \tag{20}$$

Here, the left singular matrix

$$\mathbf{U} = [u_1, u_2, \ldots, u_Y]_{N\times Y} \tag{21}$$

is the aforementioned EOF matrix $[\mathbf{E}_m(x)]$—that is, $\mathbf{Y}$ orthonormal N-dimensional EOF column vectors—thus $\mathbf{U}^{\text{T}}\mathbf{U} = \mathbf{I}_{Y\times Y}$ is the Y-dimensional identity matrix when $Y \le N$. The right singular matrix

$$\mathbf{V} = [\text{v}_1, \text{v}_2, \ldots, \text{v}_Y]_{Y\times Y} \tag{22}$$

consists of Y orthonormal Y-dimensional PC vectors, and hence $\mathbf{V}^{\text{T}}\mathbf{V} = \mathbf{I}_{Y\times Y}$ is also the Y-dimensional identity matrix. The singular eigenvalue matrix is a $Y \times Y$ diagonal matrix,

$$\mathbf{D} = \begin{bmatrix} d_1 & & \\ & \ddots & \\ & & d_Y \end{bmatrix}. \tag{23}$$

We applied the abovementioned SVD approach to the 1958–95 OGCM data to compute our monthly EOFs for each layer and for January, February, … , December. Thus, each of the 12 months has its own set of EOFs so that the seasonal cycle in temperature variance can be accounted for. Hence, our Y is 38 (i.e., from 1958 to 1995), and N is given by the third column in Table 1 for each layer, ranging from 2627 to 38 770, which is much larger than $Y = 38$.

The exact relationships between the SVD results for data matrix $[\mathbf{T}^{\text{mod}}_{\text{area}}(x, t)]$ and those for covariance matrix $\mathbf{C}(x, y) = (1/Y)\,[\mathbf{T}^{\text{mod}}_{\text{area}}(x, t)][\mathbf{T}^{\text{mod}}_{\text{area}}(y, t)]^{\text{T}}$ shown in Eqs. (3)–(5) are below:

$$[\mathbf{T}^{\text{mod}}_{\text{area}}(x, t)] = \mathbf{UDV}^{\text{T}} = [\mathbf{E}_1(x)\mathbf{E}_2(x), \ldots, \mathbf{E}_Y(x)]\mathbf{D}\{[\mathbf{T}^{\text{mod}}_{\text{area}}(x, t)][\mathbf{E}_1(x)(\mathbf{E})_2(x), \ldots, \mathbf{E}_Y(x)]\}^{\text{T}}, \tag{24}$$

that is, the right singular vectors are EOFs $\mathbf{U} = [\mathbf{E}_m(x)]$ and the left singulars vector are PCs: $\mathbf{V} = [\mathbf{T}^{\text{mod}}_{\text{area}}(x, t)][\mathbf{E}_1(x)\mathbf{E}_2(x), \ldots, \mathbf{E}_Y(x)]$, and further

$$\mathbf{\Lambda} = \begin{bmatrix} \lambda_1 & & \\ & \ddots & \\ & & \lambda_Y \end{bmatrix} = \frac{\mathbf{D}^2}{Y} = \begin{bmatrix} \frac{d_1^2}{Y} & & \\ & \ddots & \\ & & \frac{d_Y^2}{Y} \end{bmatrix} \tag{25}$$

is the diagonal eigenvalue matrix of the covariance matrix defined in Eqs. (4) and (5). This result follows the definition of the covariance matrix in Eq. (4) and its eigenvalue problem, as explained below. Substituting (24) into the eigenvalue problem of the covariance matrix yields

$$\begin{aligned}\mathbf{C}(x, y)w &= \frac{1}{Y}[\mathbf{T}^{\text{mod}}_{\text{area}}(x, t)][\mathbf{T}^{\text{mod}}_{\text{area}}(y, t)]^{\text{T}}w \\ &= \frac{1}{Y}(\mathbf{UDV}^{\text{T}})(\mathbf{UDV}^{\text{T}})^{\text{T}}w.\end{aligned} \tag{26}$$

Since $\mathbf{V}^{\text{T}}\mathbf{V} = \mathbf{I}_Y$, the matrix $\mathbf{C}$'s eigenvalue problem becomes

$$\mathbf{C}w = \frac{1}{Y}\mathbf{UD}^2(\mathbf{U}^{\text{T}}w) = \lambda w. \tag{27}$$

Multiplying both sides by $\mathbf{U}^{\text{T}}$ yields

$$\frac{1}{Y}\mathbf{U}^{\text{T}}\mathbf{UD}^2(\mathbf{U}^{\text{T}}w) = \lambda(\mathbf{U}^{\text{T}}w). \tag{28}$$

or

$$\frac{1}{Y}\mathbf{D}^2(\mathbf{U}^{\text{T}}w) = \lambda(\mathbf{U}^{\text{T}}w) \tag{29}$$

because $\mathbf{U}^{\text{T}}\mathbf{U} = \mathbf{I}_Y$. Thus, $(\mathbf{U}^{\text{T}}w)$ is an eigenvector of the diagonal matrix $(1/Y)\mathbf{D}^2$, and eigenvalues are $\lambda_1 = d_1^2/Y, \ldots, \lambda_Y = d_Y^2/Y$, which lead to Eq. (25).

Further, one can use Eq. (29) to show that EOFs are given by the $\mathbf{U}$ matrix, that is, $[\mathbf{E}_m(x)] = \mathbf{U}$ in Eq. (24). The first eigenvector $\mathbf{U}^{\text{T}}w_1$ of the diagonal matrix $(1/Y)\mathbf{D}^2$ is (1, 0, 0, …, 0). Then

Brought to you by NOAA Central Library | Unauthenticated | Downloaded 01/16/24 07:32 PM UTC

$$\mathbf{C}w_1 = \frac{1}{Y}\mathbf{U}\mathbf{D}^2(\mathbf{U}^{\mathrm{T}}w_1) = \frac{1}{Y}\mathbf{U}\begin{bmatrix} d_1^2 \\ 0 \\ \vdots \end{bmatrix}$$

$$= \frac{d_1^2}{Y}\begin{bmatrix} u_{11} \\ \vdots \\ u_{1N} \end{bmatrix} = \frac{d_1^2}{Y}\begin{bmatrix} \mathbf{E}_1(x_1) \\ \vdots \\ \mathbf{E}_1(x_N) \end{bmatrix}. \quad (30)$$

Thus, the first EOF is equal to the first right singular vector: $[\mathbf{E}_1(x)] = u_1$. The same is true for all the EOFs. Hence, $[\mathbf{E}_m(x)] = \mathbf{U}$.

For various kinds of efficient algorithms to numerically compute SVD for large matrices, see Cline and Dhillon (2006).

3. Results

a. EOFs, PCs, and eigenvalues

Figure 4 shows the 38 eigenvalues and the first three EOFs and PCs of January temperature at the model's top layer and the 100-m layer. The top layer is the 5-m layer in the OGCM, since the model cannot simulate the strict sea surface with depth zero. OGCM is a three-dimensional discretized partial differential equation model and does not have a layer of zero thickness. EOFs are computed from the JPL OGCM output aggregated to 1° latitude × 1° longitude resolution. The 100-m layer often overlaps partly with the upper portion of the thermocline layer and is partly below the mixed layer in tropical oceans. El Niño is a strong signal with very large organized spatial patterns in the mixed layer and a very large warm tongue over the eastern tropical Pacific, but it explains less variance for the 100-m layer with smaller spatial patterns (Jadhav et al. 2015). El Niño–Southern Oscillation (ENSO) explains much of the SST variation. Our first eigenvalue at the 5-m layer explains about 23% of the total variance, which is reduced to 19% for the 100-m layer (see Figs. 4a and 4b). EOF1 of the 5-m layer shows a clear, strong large-scale eastern Pacific El Niño pattern (see Fig. 4c), but the spatial pattern of EOF1 of the 100-m layer is weaker and has a smaller spatial scale not only in the tropical Pacific but also in other ocean basins. PC1 of the 5-m layer shows a large quasi-periodic variation and has an average period of 4.5 years (see Fig. 4e), while PC1 of the 100-m layer shows smaller and higher-frequency variations riding on a slow interdecadal oscillation (see Fig. 4f). This may imply that the dynamical process in the deep ocean is slower than the mixed layer and ocean surface.

EOF2 of the 5-m layer (Fig. 4g) shows the southern Pacific convergence zone from the coast of Indonesia to the coast of Chile and a significant Southern Ocean oscillation over a zonal bend between 50° and 70°S. The narrow slice of an intensive positive over the central tropical Pacific between 10°S and 10°N may be still due to ENSO. EOF2 of the 100-m layer (Fig. 4h) shows a very different pattern from that of the 5-m layer: a strong negative signal in the tropical Pacific and a strong positive signal in the tropical Atlantic. The strong modulation and asymmetry about zero in PC2 of the 5-m layer suggest stronger nonlinearity in the 5-m-layer dynamics than the dynamics of the 100-m layer (see Figs. 4i and 4j).

Our EOF3 of the 5-m layer shows the Northern Pacific and Northern Atlantic signals (Fig. 4k). However, EOF3 of the 100-m layer still shows a strong signal in the tropical Pacific and Indian Ocean (Fig. 4l). The energies reflected in the third eigenvalue and PC3 of the surface layer is smaller than those of the 100-m layer (see Figs. 4m and 4n).

We have used these EOFs for the SOG reconstruction method outlined in section 2 to reconstruct the ocean temperature data for the top 33 layers, ranging from the 5-m layer to the 5500-m layer, from January 1950 to December 2014. Although the reconstruction was made for all the layers, we present three examples, which can be easily validated by the well-known datasets, to show the success of our SOG method in ocean temperature reconstruction for both relatively dense and sparse observations:

1) January 2008, the second layer (i.e., the 10-m layer in situ observations corresponding to the 5-m layer of the OGCM): This case has good spatial sampling coverage due to the Argo data and has satellite data for verification of our reconstruction;
2) January 1998, the second layer: This case has very sparse spatial sampling coverage because the Argo network was not yet established and has a strong El Niño signal, which can be verified by both the known SST and the El Niño pattern of the reconstruction; and
3) January 1998, 100-m layer: This case also has sparse spatial coverage and shows a large pattern of strong cold anomalies in the eastern tropical Pacific.

b. Reconstructed January 2008 temperature of the second layer

Figure 5a shows excellent spatial coverage of 1° grid boxes over the global ocean. Over 3000 Argo floats helped populate this coverage. However, many boxes are still data void. Some grid boxes, although shown having data, have very few data records, which means that this fine data coverage is exaggerated due to the use of 1° grid boxes. When a finer grid is used—say,

Brought to you by NOAA Central Library | Unauthenticated | Downloaded 01/16/24 07:32 PM UTC

¼°—then the ratio of data-void grid boxes to the total number of grid boxes will be much larger. The observational data at the 10-m layer are used to anchor the first 20 EOFs computed from its corresponding OGCM's 5-m-layer temperature output.

Figure 5b shows the reconstructed second-layer temperature of January 2008, and Fig. 5c shows the NOAA ERSST of January 2008 (Huang et al. 2015; Smith et al. 2008). Although the reconstructed temperature anomalies are at surface and 10-m layers, their spatial patterns have excellent agreement with the ERSST data. The three warm zones include (i) the northern Pacific zone starting from the East China Sea to the Bering Sea; (ii) the southern Pacific zone, east of the coast of Chile, to the international date line; and (iii) the zone of the ocean region between Australia and New Zealand. A large tropical Pacific zone of cooling is also shown in both our reconstruction and satellite data. The Atlantic and Indian Ocean signals of warming and cooling are also in good agreement between the reconstruction and NOAA ERSST data. We can thus regard that the ERSST data have verified our reconstruction of temperature at the 10-m layer.

Without this reconstruction, the in situ observations, even with such good spatial coverage as shown in Fig. 5a, cannot clearly discern the warm and cold patterns, particularly the tropical Pacific cold, the warm between Australia and New Zealand, and those patterns in the Indian and Atlantic Oceans. The model-derived EOFs have thus played a critical role in mapping out the temperature's spatial patterns from the in situ observations with spatial gaps. Thus, dynamically consistent EOFs can effectively help ocean data reconstruction. The dynamic consistency is due to the conservation laws of mass, momentum, and energy in the OGCM. Consequently, the reconstructed data may be more reliable than the in situ data themselves for the same grid boxes where the number of samplings is relatively small. When a box has many accurate in situ observations, the observed data should be more reliable.

To show which EOFs are dominant in a reconstruction, Table 2 shows the estimated regression coefficients, b_m, for the mth EOF mode. The five coefficients with the largest absolute values are $b_1 = -1.91$, $b_4 = -0.89$, $b_2 = -0.71$, $b_{15} = 0.60$, and $b_3 = 0.49$. These EOF modes are heavily weighted and hence play prominent roles in the reconstruction. The large negative first mode $b_1 = -1.91$ is responsible for the major cold eastern tropical Pacific. The Southern Ocean's pattern might be due to the superposition of negative EOF2 and positive EOF3 shown in Fig. 4. These regression coefficients can help link the temporal variations to spatial variations, which may be attributed to certain physically meaningful EOF and PC modes supported by the OGCM.

c. *Reconstructed January 1998 temperature of the second and 100-m layers*

Figure 6a shows a sparse network of in situ observations of the second-layer water temperature for January 1998. This network does not have Argo data, since Argo was first proposed in 1999 (www.argo.ucsd.edu). The data were spotty and distributed off the east coast of Japan and the West Coast of the United States, and in North Atlantic, Red Sea, Mediterranean, and a few in the middle of the Pacific and Atlantic Oceans. The teleconnections of ocean water temperature enable this sparse network to sense the water temperature anomaly patterns driven by global ocean dynamics. Thus, the OGCM output is used to calculate EOFs that quantify the teleconnection patterns. SOG uses the EOFs as basis functions to interpolate the sparsely distributed point observations into a spatially coherent field of global ocean temperature anomalies. Figure 6b is a reconstruction example and displays a strong El Niño signal for January 1998. It shows the large-scale El Niño warming over the eastern tropical Pacific, South China Sea, and western Indian Ocean, which agrees well with the NOAA ERSST data (Huang et al. 2014; Smith et al. 2008) shown in Fig. 6c. Again, 20 EOFs were used in this SOG reconstruction.

Surprisingly, even the smaller-scale features of warm anomalies were also reconstructed, such as those in the region between Australia and New Zealand, from the eastern coast of Japan to Bering Sea, in the East China Sea, and near the coast of the southern tip of Chile. The reconstructed cold anomalies also agree with the ERSST data. This shows the power of SOG reconstruction, which makes such an accurate reconstruction from limited observations.

Figure 7 shows another reconstruction for the 100-m layer's temperature but for January 1998, when the in situ observations were very sparse. The observational sampling network (Fig. 7a) is similar to that for the second layer shown in Fig. 6a. Argo data were unavailable in 1998. The previous accurate reconstruction for the second layer with sparse observations helps convince one to trust this reconstruction for the 100-m layer (Fig. 7b).

A distinct feature is shown in Fig. 7b: a large western tropical Pacific region with very strong cold anomalies reaching −5°C. The region stretches from the east coasts of Indonesia and Australia (150°E) to 140°W, a zonal band of more 7000 km long. Similar cold anomalies appeared in our reconstruction for the 100-m-layer temperature in all the other El Niño events, such as January 1983 (see animation at http://shen.sdsu.edu/100mtemp.mov).

Brought to you by NOAA Central Library | Unauthenticated | Downloaded 01/16/24 07:32 PM UTC

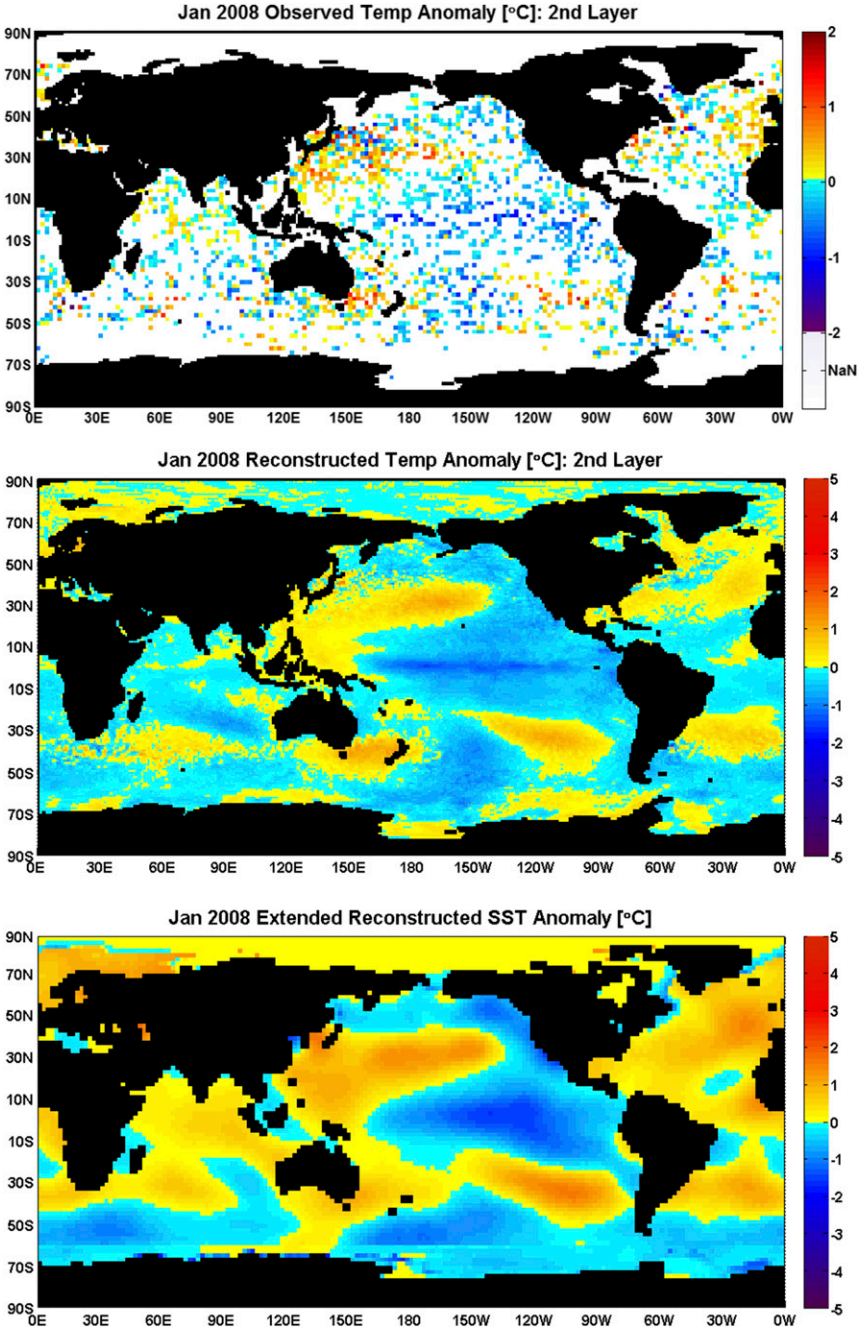

FIG. 5. (a) The observed January 2008 temperature anomalies for the second layer. (b) The SOG reconstructed January 2008 temperature for the same layer using 20 EOF modes. (c) NOAA ERSST data (Huang et al. 2015).

Roemmich and Gilson (2011) examined 2004–11 Argo data and concluded that for the 2 years prior to the 2009 El Niño, the top 0–100-dbar ocean layer gained heat, while the subsurface 100–500-dbar layer lost the similar amount of heat. Their finding suggested the existence of substantial subsurface cold anomalies, which are large in both temperature magnitude and space area and counter the large surface El Niño warm anomalies over the eastern tropical Pacific. Our reconstruction hence has provided detailed spatiotemporal structure of the subsurface El Niño cold anomalies, rather than only the surface El Niño warm anomalies commonly shown in existing literature.

Brought to you by NOAA Central Library | Unauthenticated | Downloaded 01/16/24 07:32 PM UTC

TABLE 2. The 20 b_n for our three reconstruction examples: second layer in January 2008 and January 1998, and 100-m layer in January 1998.

Layer	Time	b_1	b_2	b_3	b_4	b_5	b_6	b_7	b_8	b_9	b_{10}
Top	Jan 2008	−1.91	−0.71	0.49	−0.89	−0.15	0.37	0.03	−0.63	−0.23	0.36
Top	Jan 1998	3.50	−0.87	0.58	−0.66	1.38	0.59	0.82	−0.40	1.20	0.31
100 m	Jan 1998	4.10	3.03	1.69	−2.79	0.15	3.30	0.07	−0.42	0.46	−0.01
Layer	Time	b_{11}	b_{12}	b_{13}	b_{14}	b_{15}	b_{16}	b_{17}	b_{18}	b_{19}	b_{20}
Top	Jan 2008	0.04	−0.11	−0.29	−0.16	0.60	−0.27	0.07	0.20	0.06	−0.14
Top	Jan 1998	−0.03	0.31	0.04	−0.46	0.24	−0.13	−0.71	−0.81	0.34	0.07
100 m	Jan 1998	−1.41	0.05	−0.41	1.08	0.51	−0.04	0.81	1.13	0.21	0.16

The western Pacific cold anomalies for January 1998 at the second layer were small, between −1° and 0°C, and limited to the west of the international date line (see Fig. 7b). They got enhanced at the 100-m layer or deeper and formed a large area of strong cold anomalies.

The warm anomaly side of the El Niño signal at the surface layer over the extended eastern tropical Pacific got reduced in both size of the region and the magnitude of the anomalies. Figure 7b shows that the El Niño warming the 100-m layer retracted only to the very east of the Pacific, east of 120°W, the coast of Peru and Columbia, and the coast of California. The warm anomalies were also weaker than those of the second layer. Most of the tropical Pacific's warming for the second layer appeared at the 100-m layer.

The western Pacific's El Niño cold gets enhanced and the eastern Pacific's El Niño warm anomalies retract as the depth increases from the ocean surface to the subsurface. This structure of temperature anomalies may be related to the shoaling of the thermocline in the western Pacific during an El Niño process. The thermocline's rise in the west and the drop in the east of the tropical Pacific balance the oceanic heat anomalies in the surface and the subsurface.

d. Reconstruction errors and validations

This subsection discusses the square errors in Eq. (12), which are also called residuals. The sum with an area factor is the SSE whose minimization yields our regression algorithm. We ask what are the sizes and spatial distributions of the regression residuals in our SOG reconstruction. An example is used to illustrate the residual errors: January 1998's second layer. Systematic studies on the error estimation and statistical inferences (Shen et al. 2004), such as the map of the error variance for $e(x, t)$, and the detailed analysis on the significance of the EOF coefficients, involve more theory of multivariate regression and belong to another paper.

Figure 8 shows differences between January 1998's layer temperature anomalies and the reconstructed anomalies—that is, regression residuals—as a measure of reconstruction errors. The sum of the squares of these differences with an area factor is the SSE shown in Eq. (12). Figure 8 shows that positive and negative, and large and small residuals are all mixed in any given oceanic region with data, although the residuals over the North Sea seem to have a large magnitude, which is likely due to larger temperature variances at a higher-latitude region. This implies the nonexistence of a systematic bias from either reconstruction or observation. Thus, we may regard that positive and negative residuals are randomly distributed because no particular region has consistently large bias errors, and the observational data have consistent quality without systematic biases. Some grid boxes' residuals are large, which do not necessarily suggest large reconstruction errors, because the large residuals may be due to the inaccurate climatology and hence inaccurate anomalies computed from the in situ data. As mentioned earlier, some grid boxes' climatology was computed using very few samples—say, 2 or 3—which do not accurately represent the true climatology and hence distort the anomalies. The large residuals may also be due to the sampling errors of the gridbox data, which were aggregated from very few records in a space–time box of 2° latitude × 2° longitude by one month in time.

The outliers of residuals are marked with stars in Fig. 8 and are outside the interval (−2, 2)°C. Only three grid boxes have these outliers in the northern Atlantic, east of Halifax, and the Baltic Sea. One value is positive and two are negative. Again, the outliers do not show systematic biases of the observed data either.

We also compared our SOG reconstruction with the data assimilation products of NCEP's GODAS and checked with the University of Maryland's SODA. Figure 9 shows an example of a comparison between our SOG reconstruction for January 1998 on a cross section along the equator and GODAS. In the top 300 m, the SOG and GODAS data agree well over the Pacific, a warm eastern tropical Pacific surface over a cold western tropical Pacific, but have clear differences over the Indian and

Brought to you by NOAA Central Library | Unauthenticated | Downloaded 01/16/24 07:32 PM UTC

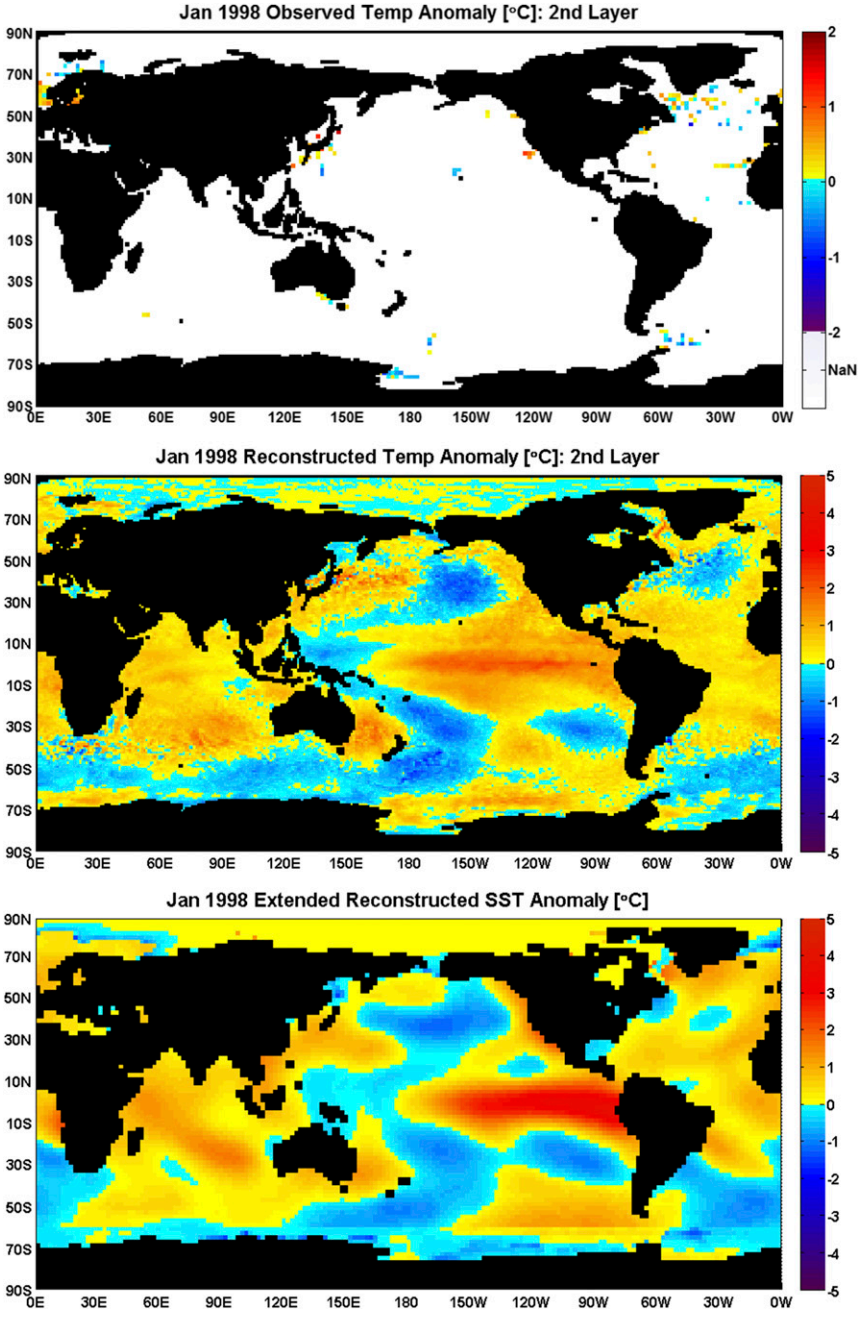

FIG. 6. As in Fig. 5, but for January 1998.

Atlantic Oceans. In the Indian Ocean, GODAS has a large-scale strong warm anomaly around 100 m, but SOG does not, and it even has a small-scale pocket of cold anomaly. In the Atlantic, the SOG's top warm water layer is about 100 m thick, while the thickness of the corresponding GODAS layer is only about 50 m. Below 300 m, the SOG and GODAS data agree better in the Pacific Ocean than in the Atlantic and Indian Oceans. However, the temperature variations in that depth are small. Thus, the differences are small too, often within 0.5°C. Although we cannot conclude here which dataset is more accurate, we can still say that SOG's surface water temperature along the equator appears to be more realistic: the SOG shows a weak complete Indian Ocean surface warm anomaly supported by ERSST. The existing GODAS has extensive validation results, including validation against dependent and independent data, salinity, and U current correlation. Our SOG product can serve as a convenient

Brought to you by NOAA Central Library | Unauthenticated | Downloaded 01/16/24 07:32 PM UTC

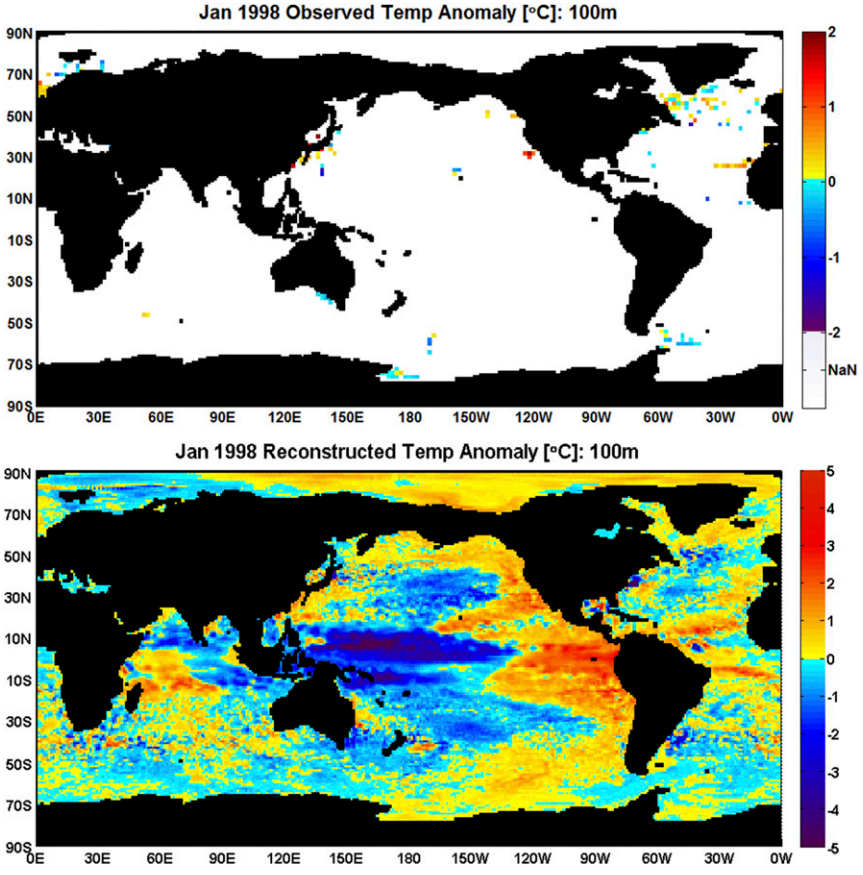

FIG. 7. As in Fig. 6, but for the 100-m layer and without the SST data.

validation dataset for the GODAS's continuous operational validation procedures in the future.

Another validation is to use SOG to reconstruct the JPL OGCM temperature for a given month and a given layer using historical sampling locations. We particularly examined three cases: January 1959, which is inside the SVD data's temporal domain of 1958–95; January 1998 at the 200-m layer with very sparse sampling; and January 2008 at the second layer with dense sampling. The January 1959 reconstruction is almost a perfect replication of the JPL OGCM output (figures not shown in this paper). This is expected and can be mathematically

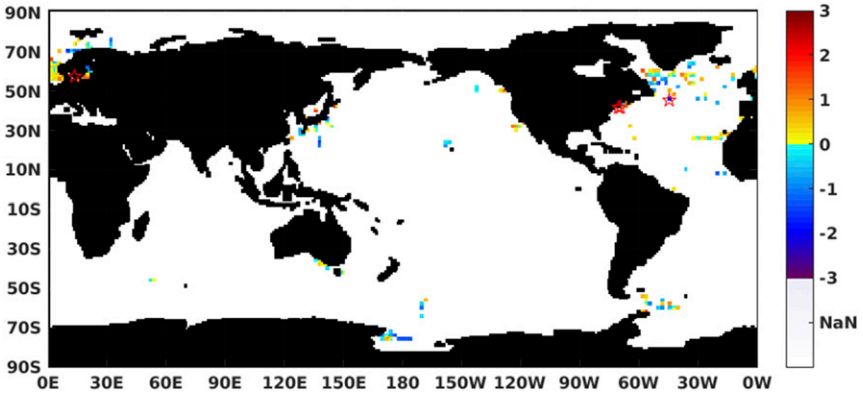

FIG. 8. Residual errors of the SOG regression reconstruction for January 1998's second-layer temperature: observed anomalies minus the reconstructed anomalies. The outlier residuals outside of the interval (−2, 2)°C are marked with stars.

Brought to you by NOAA Central Library | Unauthenticated | Downloaded 01/16/24 07:32 PM UTC

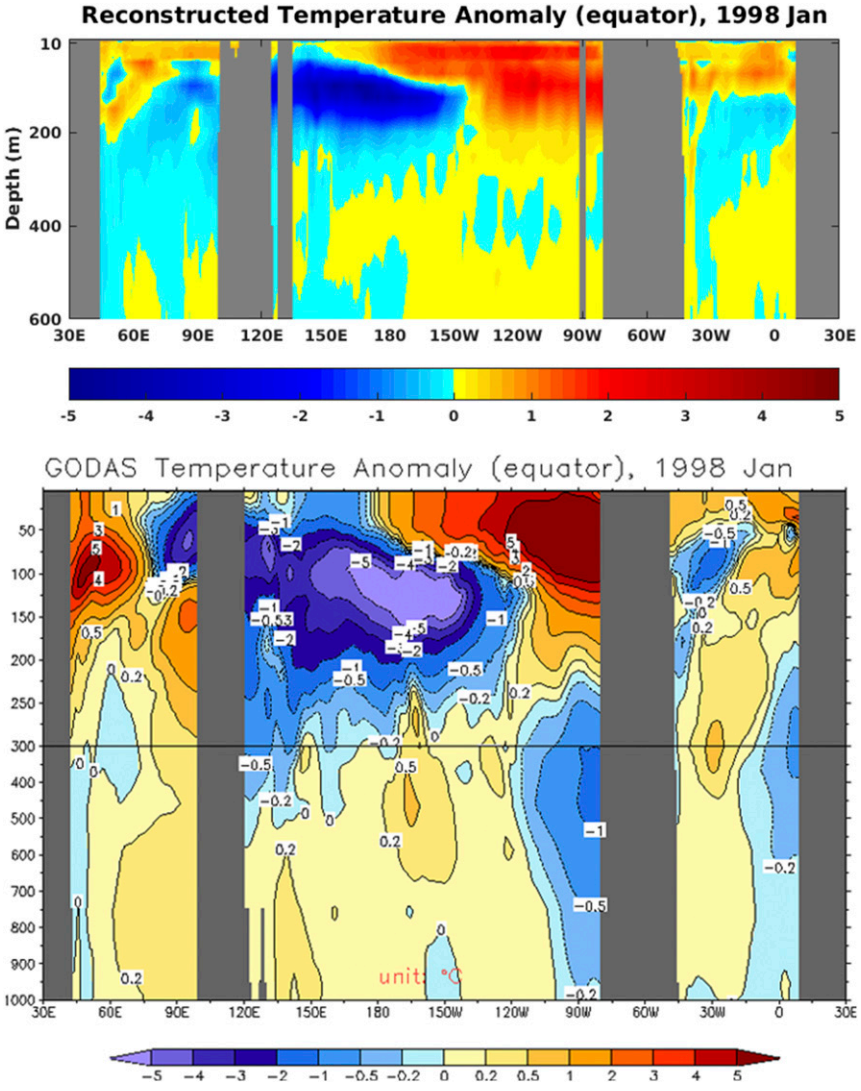

FIG. 9. Comparison between (a) the SOG reconstruction and (b) the NCEP GODAS oceanic reanalysis product. Please note that the vertical scales are different for the two panels when deeper than 300 m.

proved rigorously, since the January 1959 OGCM output was included to generate the EOFs. The January 2008 SOG reconstruction for the second layer can also recover the OGCM data very well except for the small-scale coastal variations (not shown in this paper either). Figure 10 compares the January 1998 200-m-layer SOG reconstruction with the JPL OGCM output as the ''observed truth.'' The figures shows that SOG can still recover the main features of the eastern tropical Pacific's cold anomalies, warm–cold patterns in Atlantic and Indian Oceans, but it fails to recover the OGCM's strong warm anomaly off the coast of Ecuador and Peru.

A mathematical question on validation is whether the EOFs can form a complete basis so that all the possible oceanic temperature profiles can be decomposed into the EOFs. Our EOFs from JPL OGCM may be regarded as the eigenfunctions of a self-adjoint differential operator (Song and Hou 2006) and can form a complete basis for a functional space that contains all the possible ocean temperature profiles. However, the convergence rate of the EOF expansion in Eq. (13) may vary from year to year. Although they are ideally to appear in the coefficients of higher order EOFs, errors from the observational data may enter the expansion early in the first a few modes. Thus, in practical reconstruction, certain temperature profiles, such as very small-scale coastal variations around Japan, may be missed.

The gridded $2° \times 2°$ latitude–longitude data have errors, including sampling errors, random observational errors,

Brought to you by NOAA Central Library | Unauthenticated | Downloaded 01/16/24 07:32 PM UTC

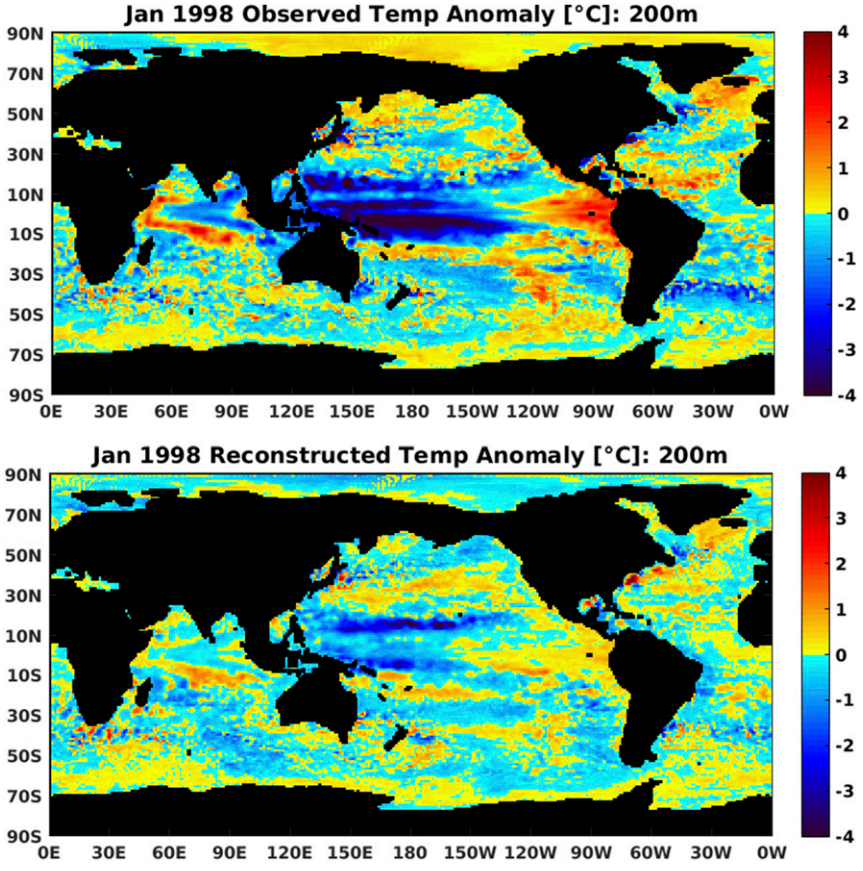

FIG. 10. Comparison between (a) the JPL OGCM January 1998 200-m layer temperature as the observed truth and (b) its SOG reconstruction using the data at the January 1998 sampling locations.

and possible observational biases (Smith et al. 2013). Future uncertainty quantification for the SOG products may consider these errors using the correlation-factor method (Shen et al. 2007, 2012; Wang et al. 2014).

4. Conclusions and discussion

We have used the SOG method to make dynamically consistent reconstruction of ocean temperature at different levels. The dynamical consistency is achieved by using the basis of EOF derived from NASA JPL non-Boussinesq OGCM output at ¼° resolution. An efficient algorithm of singular value decomposition (SVD) method is used to calculate the EOFs to enable efficient computing when the spatial resolution is very high. These EOFs are used as explainable variables and regressed against the sparsely distributed gridded ocean water temperature observations at 33 standard depth levels, from the top surface layer to the layer of 5500 m. The observed data span from 1950 to 2014, and have dense sampling during the periods of Tropical-Ocean Global Atmosphere (TOGA) (1985–1995) and Argo (2000–present) (Fig. 1b). Most observations are confined to the upper ocean, and the number of samples decreases rapidly with depth, falling below 100 000 profiles at 2000 m and even less in the deeper layers (Fig. 2). Analysis of these temperature profiles has produced a climatology and also a monthly temperature time series on $2° \times 2°$ grid boxes wherever in situ data are available from 1950 to 2014. Our reconstructions are then made on the anomalies relative to this climatology.

The ¼° NASA JPL OGCM output has been upscaled onto a 1° grid, and the 2° observational data are downscaled to the same 1° grid. The spatial domain is the entire global ocean, while the temporal domain is from January 1958 to December 2013. The data are read into a two-dimensional $N \times Y$ matrix, with rows indexing the grid box locations, and columns indexing months. An area-weighted multivariate regression approach is applied to the 1° gridded data with the EOFs, computed by the SVD method for the space–time OGCM data, as

Brought to you by NOAA Central Library | Unauthenticated | Downloaded 01/16/24 07:32 PM UTC

the explainable variables. The reconstruction steps are described in section 2. Three temperature reconstruction examples are presented: January 2008 and January 1998 at the top surface layer and January 1998 at the 100-m layer. The two surface-layer reconstructions are verified by independent satellite observations and are considered very reliable. The 100-m-layer reconstruction shows that the January 1998 El Niño's warm signal retracts from 160°E at the western Pacific at the surface to 130°W at the eastern Pacific at the 100-m layer, off the coast of Columbia and Peru. In contrast, El Niño's cold anomalies on the ocean surface over a small area off the coast of Indonesia get enhanced to −5°C at the 100-m layer and extended from 150°E to 140°W, stretching more than 7000 km long in an east–west direction. A simple error analysis on regression residuals indicates that there are no systematic biases in either the observed data or the reconstructed data. Figure 6 shows good agreement between the January 1998 ERSST and the second-layer temperature reconstructed by SOG with less than 0.4% data coverage. This shows the power of the SOG reconstruction method.

Although our surface-layer reconstruction has been verified by ERSST data and residual errors of reconstruction have been shown for a case, these are far from a systematic estimate of reconstruction errors. For example, the SOG reconstruction and the ERSST shown in Fig. 6 have apparent differences. ERSST's eastern tropical Pacific warm anomaly band is narrower than that of the SOG reconstruction, but it has a larger magnitude. A comprehensive study about the uncertainties in the reconstructed products based on the multivariate regression theory and the model data and observed data used here will be included in follow-up papers. Future papers will also include results of the reconstructed ocean salinity using a similar approach. We will further show the physics implied from a suite of reconstructed products.

We would like to clarify that although it uses ocean models, our SOG method is different from the data assimilation approach, whose output is essentially the model results corrected by observational data. Our gridded output is faithful to the observational data and is consistent with ocean circulation patterns derived from the non-Boussinesq OGCM.

Another point of discussion is about the best choice of EOF truncation number M. Shen et al. (2001) also looked for the optimal number of modes from the point of view of EOF errors and showed the difficulty of finding an optimal M. Here, let us use two special cases to discuss the subtlety of the choice: one is overfit and another underfit.

The first special case is that we have N_d years of OGCM simulations, rather than 38 years from 1958 to 1995. Then, N_d EOFs can be computed and N_d in situ data can be perfectly fitted by using these N_d EOF modes,

$$[\hat{\mathbf{T}}(x,t)]_{N\times 1} = [\mathbf{\Psi}(x)]_{N\times N_d}\{[\mathbf{\Psi}(x_d)]^{-1}\}_{N_d\times N_d}[\mathbf{D}(x_d,t)]_{N_d\times 1}, \tag{31}$$

if the matrix inversion exists. Here, each column of $[\mathbf{\Psi}(x)]$ is an EOF. In this case, $\hat{\mathbf{T}}(x_d, t) = \mathbf{D}(x_d, t)$; thus, SSE = 0 according to the SSE definition Eq. (12). It is an overfit, if N_d is a reasonably large number, say, 300. Higher EOFs are noisy and do not have physical meaning because higher EOFs' corresponding eigenvalues are too close to each other, and higher EOFs thus have large errors. The mth EOF's error is proportional to $1/(\lambda_m - \lambda_{m+1})$, while $\lambda_m - \lambda_{m+1}$ is almost zero, according to North's rule of thumb (Shen et al. 2001). Therefore, over fit is bad because of the errors of in situ data and the noise of the higher-order EOF modes.

Another special case is only one observation and it can use only one EOF mode,

$$[\hat{\mathbf{T}}(x,t)]_{N\times 1} = \frac{\mathbf{D}(x_1,t)}{\boldsymbol{\psi}_1(x_1)}\boldsymbol{\psi}_1(x), \tag{32}$$

when $\boldsymbol{\psi}(x_1) \neq 0$. Physically, it is an underfit, since the detailed resolutions in the higher EOFs are not included in the reconstruction. However, the SSE for this is zero for this single observation. So, statistically this is an "overfit" in the sense of SSE = 0.

The real situation is that we have N_d observations to determine M EOFs, which are not very noisy, where $N_d > M$, so the regression is for an overdetermined system, that is, more observations than the number of unknowns. Therefore, we should look for the best number of EOFs for a given $N_d > 1$. In practice, we usually choose M so that 90% of the variance is explained by the first M EOF modes (Smith et al. 2013; Shen et al. 2014). This choice solely depends on OGCM physics and has ignored the observations. Smith et al. (1998) introduced the screening method to select an EOF mode. If the observations do not support the EOF, then the EOF is still excluded even if it is within the 90% of variance explained (Smith et al. 1998). A balance of the over fit (including too many EOF modes and resulting in a very small SSE) and model simplicity (including too few EOF modes and resulting in a large SSE and unresolved small-scale spatial patterns) may be measured by the minimization of

$$\ln\hat{\sigma}^2 + 2M. \tag{33}$$

This is a function of the total number of EOF modes, M. The function is concave up and hence has a minimum.

Brought to you by NOAA Central Library | Unauthenticated | Downloaded 01/16/24 07:32 PM UTC

This minimum reflects the balance of overfit and simplicity and is the Akaike information criterion (AIC). A stepwise multiple regression model may be used to incorporate the AIC (Rawlings et al. 2001). Thus, our SOG approach helps open many new problems in data reconstruction, data connection to physical mechanisms, and uncertainty quantification for various kinds of climate parameters.

Acknowledgments. This study was supported in part by a contract from the NASA Jet Propulsion Laboratory, and by grants from the U.S. National Science Foundation (Award AGS-1419526) and the U.S. National Oceanic and Atmospheric Administration (Award 13342-Z7812001). Tangdong Qu's work is supported by grants from the NASA Aquarius Science Team investigation (Award NNX16AE10G) and Physical Oceanography program (Award NNX16AH86G). Tony Song's work is carried out at the Jet Propulsion Laboratory, California Institute of Technology, under contract with NASA. In situ data are obtained from the University of Hawaii, where L. Zhang assisted with some analysis of the in situ data.

REFERENCES

Abraham, J. P., and Coauthors, 2013: A review of global ocean temperature observations: Implications for ocean heat content estimates and climate change. *Rev. Geophys.*, **51**, 450–483, doi:10.1002/rog.20022.

Anderson, J. E., and S. C. Riser, 2014: Near-surface variability of temperature and salinity in the near-tropical ocean: Observations from profiling floats. *J. Geophys. Res. Oceans*, **119**, 7433–7448, doi:10.1002/2014JC010112.

Azaneu, M., R. Kerr, M. M. Mata, and C. A. Garcia, 2013: Trends in the deep Southern Ocean (1958–2010): Implications for Antarctic Bottom Water properties and volume export. *J. Geophys. Res. Oceans*, **118**, 4213–4227, doi:10.1002/jgrc.20303.

Balmaseda, M. A., K. E. Trenberth, and E. Källén, 2013: Distinctive climate signals in reanalysis of global ocean heat content. *Geophys. Res. Lett.*, **40**, 1754–1759, doi:10.1002/grl.50382.

Bamber, J., M. den Broeke, J. Ettema, J. Lenaerts, and E. Rignot, 2012: Recent large increases in freshwater fluxes from Greenland into the North Atlantic. *Geophys. Res. Lett.*, **39**, L19501, doi:10.1029/2012GL052552.

Cabanes, C., and Coauthors, 2013: The CORA dataset: Validation and diagnostics of in-situ ocean temperature and salinity measurements. *Ocean Sci.*, **9**, 1–18, doi:10.5194/os-9-1-2013.

Carton, J. A., and B. S. Giese, 2008: A reanalysis of ocean climate using Simple Ocean Data Assimilation (SODA). *Mon. Wea. Rev.*, **136**, 2999–3017, doi:10.1175/2007MWR1978.1.

Chen, X., Y. Feng, and N. E. Huang, 2014: Global sea level trend during 1993–2012. *Global Planet. Change*, **112**, 26–32, doi:10.1016/j.gloplacha.2013.11.001.

Cline, A. K., and I. S. Dhillon, 2006: Computation of the singular value decomposition. *Handbook of Linear Algebra*, L. Hogben, Ed., Chapman and Hall/CRC, 45-1–45-13, doi:10.1201/9781420010572.ch45.

Demmel, J., and W. Kahan, 1990: Accurate singular values of bidiagonal matrices. *SIAM J. Sci. Stat. Comput.*, **11**, 873–912, doi:10.1137/0911052.

Desbruyères, D. G., E. L. McDonagh, B. A. King, F. K. Garry, A. T. Blaker, B. I. Moat, and H. Mercier, 2014: Full-depth temperature trends in the northeastern Atlantic through the early 21st century. *Geophys. Res. Lett.*, **41**, 7971–7979, doi:10.1002/2014GL061844.

Dunstone, N. J., 2014: A perspective on sustained marine observations for climate modelling and prediction. *Philos. Trans. Roy. Soc. London*, **372A**, 20130340, doi:10.1098/rsta.2013.0340.

Durack, P. J., P. J. Gleckler, F. W. Landerer, and K. E. Taylor, 2014: Quantifying underestimates of long-term upper-ocean warming. *Nat. Climate Change*, **4**, 999–1005, doi:10.1038/nclimate2389.

Gasparin, F., D. Roemmich, J. Gilson, and B. Cornuelle, 2015: Assessment of the upper-ocean observing system in the equatorial Pacific: The role of Argo in resolving intraseasonal to interannual variability. *J. Atmos. Oceanic Technol.*, **32**, 1668–1688, doi:10.1175/JTECH-D-14-00218.1.

Gille, S. T., 2002: Warming of the Southern Ocean since the 1950s. *Science*, **295**, 1275–1277, doi:10.1126/science.1065863.

——, 2008: Decadal-scale temperature trends in the Southern Hemisphere ocean. *J. Climate*, **21**, 4749–4765, doi:10.1175/2008JCLI2131.1.

Greatbatch, R. J., 1994: A note on the represent of steric sea level in models that conserve volume rather than mass. *J. Geophys. Res.*, **99**, 12 767–12 771, doi:10.1029/94JC00847.

Gregory, J. M., and J. A. Lowe, 2000: Predictions of global and regional sea-level rise using AOGCMs with and with flux adjustment. *Geophys. Res. Lett.*, **27**, 3069–3072, doi:10.1029/1999GL011228.

Griffies, S. M., and R. J. Greatbatch, 2012: Physical processes that impact the evolution of global mean sea level in ocean climate models. *Ocean Modell.*, **51**, 37–72, doi:10.1016/j.ocemod.2012.04.003.

Haidvogel, D. B., and Coauthors, 2008: Ocean forecasting in terrain-following coordinates: Formulation and skill assessment of the Regional Ocean Modeling System. *J. Comput. Phys.*, **227**, 3595–3624, doi:10.1016/j.jcp.2007.06.016.

Hansen, J., and Coauthors, 2005: Earth's energy imbalance: Confirmation and implications. *Science*, **308**, 1431–1435, doi:10.1126/science.1110252.

——, M. Sato, P. Kharecha, and K. V. Schuckmann, 2011: Earth's energy imbalance and implications. *Atmos. Chem. Phys.*, **11**, 13 421–13 449, doi:10.5194/acp-11-13421-2011.

Huang, B., and Coauthors, 2015: Extended reconstructed sea surface temperature version 4 (ERSST. v4). Part I: Upgrades and intercomparisons. *J. Climate*, **28**, 911–930, doi:10.1175/JCLI-D-14-00006.1.

Huang, R. X., and X. Jin, 2002: Deep circulation in the South Atlantic induced by bottom-intensified mixing over the mid-ocean ridge. *J. Phys. Oceanogr.*, **32**, 1150–1164, doi:10.1175/1520-0485(2002)032<1150:DCITSA>2.0.CO;2.

Ishii, M., and M. Kimoto, 2009: Reevaluation of historical ocean heat content variations with time-varying XBT and MBT depth bias corrections. *J. Oceanogr.*, **65**, 287–299, doi:10.1007/s10872-009-0027-7.

Jadhav, J., S. Panickal, S. Marathe, and K. Ashok, 2015: On the possible cause of distinct El Nino types in the recent decades. *Sci. Rep.*, **5**, 17 009, doi:10.1038/srep17009.

Johnson, G. C., J. M. Lyman, and N. G. Loeb, 2016: Improving estimates of Earth's energy imbalance. *Nat. Climate Change*, **6**, 639–640, doi:10.1038/nclimate3043.

Brought to you by NOAA Central Library | Unauthenticated | Downloaded 01/16/24 07:32 PM UTC

Johnson, R. A., and D. W. Wichern, 2007: *Applied Multivariate Statistical Analysis*. 6th ed. Pearson Prentice Hall, 773 pp.

Kaplan, A., M. A. Cane, Y. Kushnir, A. C. Clement, M. B. Blumenthal, and B. Rajagopalan, 1998: Analyses of global sea surface temperature 1856–1991. *J. Geophys. Res.*, **103**, 18 567–18 589, doi:10.1029/97JC01736.

Leuliette, E. W., 2011: The balancing of the sea-level budget. *Curr. Climate Change Rep.*, **1**, 185–191, doi:10.1007/s40641-015-0012-8.

——, and L. Miller, 2009: Closing the sea level rise budget with altimetry, Argo, and GRACE. *Geophys. Res. Lett.*, **36**, L04608, doi:10.1029/2008GL036010.

Levitus, S., J. Antonov, and T. Boyer, 2005: Warming of the world ocean, 1955–2003. *Geophys. Res. Lett.*, **32**, L02604, doi:10.1029/2004GL021592.

——, and Coauthors, 2012: World ocean heat content and thermosteric sea level change (0–2000 m), 1955–2010. *Geophys. Res. Lett.*, **39**, L10603, doi:10.1029/2012GL051106.

Llovel, W., J. K. Willis, F. W. Landerer, and I. Fukumori, 2014: Deep-ocean contribution to sea level and energy budget not detectable over the past decade. *Nat. Climate Change*, **4**, 1031–1035, doi:10.1038/nclimate2387.

Locarnini, R. A., A. V. Mishonov, J. I. Antonov, T. P. Boyer, H. E. Garcia, O. K. Baranova, M. M. Zweng, and D. R. Johnson, 2010: *Temperature*. Vol. 1, *World Ocean Atlas 2009*, NOAA Atlas NESDIS 68, 184 pp.

Loeb, N. G., J. M. Lyman, G. C. Johnson, R. P. Allan, D. R. Doelling, T. Wong, B. J. Soden, and G. L. Stephens, 2012: Observed changes in top-of-the-atmosphere radiation and upper-ocean heating consistent within uncertainty. *Nat. Geosci.*, **5**, 110–113, doi:10.1038/ngeo1375.

Lyman, J. M., S. A. Good, V. V. Gouretski, M. Ishii, G. C. Johnson, M. D. Palmer, D. M. Smith, and J. K. Willis, 2010: Robust warming of the global upper ocean. *Nature*, **465**, 334–337, doi:10.1038/nature09043.

Mauritzen, C., A. Melsom, and R. T. Sutton, 2012: Importance of density-compensated temperature change for deep North Atlantic Ocean heat uptake. *Nat. Geosci.*, **5**, 905–910, doi:10.1038/ngeo1639.

Meehl, G. A., J. M. Arblaster, J. T. Fasullo, A. Hu, and K. E. Trenberth, 2011: Model-based evidence of deep-ocean heat uptake during surface-temperature hiatus periods. *Nat. Climate Change*, **1**, 360–364, doi:10.1038/nclimate1229.

Milne, G. A., W. R. Gehrels, C. W. Hughes, and M. A. Tamisiea, 2009: Identifying the causes of sea-level change. *Nat. Geosci.*, **2**, 471–478, doi:10.1038/ngeo544.

Mishonov, A. V., and Coauthors, 2013: *Temperature*. Vol. 1, *World Ocean Atlas 2013*, NOAA Atlas NESDIS 73, 40 pp.

Moon, J.-H., and Y. T. Song, 2013: Sea level and heat content changes in the western North Pacific. *J. Geophys. Res. Oceans*, **118**, 2014–2022, doi:10.1002/jgrc.20096.

——, ——, P. D. Bromirski, and A. J. Miller, 2013: Multidecadal regional sea level shifts in the Pacific over 1958–2008. *J. Geophys. Res. Oceans*, **118**, 7024–7035, doi:10.1002/2013JC009297.

Murphy, D. M., S. Solomon, R. W. Portmann, K. H. Rosenlof, P. M. Forster, and T. Wong, 2009: An observationally based energy balance for the Earth since 1950. *J. Geophys. Res.*, **114**, D17107, doi:10.1029/2009JD012105.

Purkey, S. G., and G. C. Johnson, 2010: Warming of global abyssal and deep Southern Ocean waters between the 1990s and 2000s: Contributions to global heat and sea level rise budgets. *J. Climate*, **23**, 6336–6351, doi:10.1175/2010JCLI3682.1.

Qu, T., H. Mitsudera, and T. Yamagata, 1999: A climatology of the circulation and water mass distribution near the Philippine coast. *J. Phys. Oceanogr.*, **29**, 1488–1505, doi:10.1175/1520-0485(1999)029<1488:ACOTCA>2.0.CO;2.

——, L. Zhang, and N. Schneider, 2016: North Atlantic subtropical underwater and its year-to-year variability in annual subduction rate during the Argo period. *J. Phys. Oceanogr.*, **46**, doi:10.1175/JPO-D-15-0246.1.

Rawlings, J. O., S. G. Pantula, and D. A. Dickey, 2001: *Applied Regression Analysis: A Research Tool*. 2nd ed. Springer, 651 pp.

Rayner, N. A., D. E. Parker, E. B. Horton, C. K. Folland, L. V. Alexander, D. P. Rowell, E. C. Kent, and A. Kaplan, 2003: Global analyses of sea surface temperature, sea ice, and night marine air temperature since the late nineteenth century. *J. Geophys. Res.*, **108**, 4407, doi:10.1029/2002JD002670.

Roemmich, D., and J. Gilson, 2011: The global ocean imprint of ENSO. *Geophys. Res. Lett.*, **38**, L13606, doi:10.1029/2011GL047992.

——, and G. C. Johnson, 2012: Recent progress and the current status of global ocean observations of temperature, heat content, and steric sea level. Interagency Ocean Observation Committee Rep., 8 pp. [Available online at http://www.iooc.us/wp-content/uploads/2012/06/Draft-Temp-Heat-Content-steric-sea-level.pdf.]

——, W. J. Gould, and J. Gilson, 2012: 135 years of global ocean warming between the *Challenger* expedition and the Argo Programme. *Nat. Climate Change*, **2**, 425–428, doi:10.1038/nclimate1461.

——, J. Church, J. Gilson, D. Monselesan, P. Sutton, and S. Wijffels, 2015: Unabated planetary warming and its ocean structure since 2006. *Nat. Climate Change*, **5**, 240–245, doi:10.1038/nclimate2513.

Shchepetkin, A., and J. C. McWilliams, 2005: The regional oceanic modeling system (ROMS): A split-explicit, free-surface, topography-following-coordinate oceanic model. *Ocean Modell.*, **9**, 347–404, doi:10.1016/j.ocemod.2004.08.002.

Shen, S. S. P., T. M. Smith, C. F. Ropelewski, and R. E. Livezey, 1998: An optimal regional averaging method with error estimates and a test using tropical Pacific SST data. *J. Climate*, **11**, 2340–2350, doi:10.1175/1520-0442(1998)011<2340:AORAMW>2.0.CO;2.

——, W. K. M. Lau, K.-M. Kim, and G. Li, 2001: A canonical ensemble correlation prediction model for seasonal precipitation anomaly. NASA Tech. Memo. NASA-TM-2001-209989, 53 pp. [Available online at http://ntrs.nasa.gov/archive/nasa/casi.ntrs.nasa.gov/20010102849.pdf.]

——, A. N. Basist, G. Li, C. Williams, and T. R. Karl, 2004: Prediction of sea surface temperature from the Global Historical Climatology Network data. *Environmetrics*, **15**, 233–249, doi:10.1002/env.638.

——, H. Yin, and T. M. Smith, 2007: An estimate of the error variance of the gridded GHCN monthly surface air temperature data. *J. Climate*, **20**, 2321–2331, doi:10.1175/JCLI4121.1.

——, C. K. Lee, and J. Lawrimore, 2012: Uncertainties, trends, and hottest and coldest years of U.S. surface air temperature since 1895: An update based on the USHCN V2 TOB data. *J. Climate*, **25**, 4185–4203, doi:10.1175/JCLI-D-11-00102.1.

——, N. Tafolla, T. M. Smith, and P. A. Arkin, 2014: Multivariate regression reconstruction and its sampling error for the quasi-global annual precipitation from 1900 to 2011. *J. Atmos. Sci.*, **71**, 3250–3268, doi:10.1175/JAS-D-13-0301.1.

Brought to you by NOAA Central Library | Unauthenticated | Downloaded 01/16/24 07:32 PM UTC

Smith, T. M., R. W. Reynolds, R. E. Livezey, and D. C. Stokes, 1996: Reconstruction of historical sea surface temperatures using empirical orthogonal functions. *J. Climate*, **9**, 1403–1420, doi:10.1175/1520-0442(1996)009<1403:ROHSST>2.0.CO;2.

——, R. E. Livezey, and S. S. P. Shen, 1998: An improved method for analyzing sparse and irregularly distributed SST data on a regular grid: The tropical Pacific Ocean. *J. Climate*, **11**, 1717–1729, doi:10.1175/1520-0442(1998)011<1717:AIMFAS>2.0.CO;2.

——, R. W. Reynolds, T. C. Peterson, and J. Lawrimore, 2008: Improvements to NOAA's historical merged land–ocean temperature analysis (1880–2006). *J. Climate*, **21**, 2283–2296, doi:10.1175/2007JCLI2100.1.

——, S. S. P. Shen, L. Ren, and P. A. Arkin, 2013: Estimating monthly precipitation uncertainty beginning 1900. *J. Atmos. Oceanic Technol.*, **30**, 1107–1122, doi:10.1175/JTECH-D-12-00197.1.

Song, Y., and D. Haidvogel, 1994: A semi-implicit primitive equation ocean circulation model using a generalized topography-following coordinate system. *J. Comput. Phys.*, **115**, 228–244, doi:10.1006/jcph.1994.1189.

Song, Y. T., and T. Y. Hou, 2006: Parametric vertical coordinate formulation for multiscale, Boussinesq, and non-Boussinesq ocean modeling. *Ocean Modell.*, **11**, 298–332, doi:10.1016/j.ocemod.2005.01.001.

——, and F. Colberg, 2011: Deep ocean warming assessed from altimeters, Gravity Recovery and Climate Experiment, in situ measurements, and a non-Boussinesq ocean general circulation model. *J. Geophys. Res.*, **116**, C02020, doi:10.1029/2010JC006601.

——, R. Gross, X. Wang, and V. Zlotnicki, 2010: A non-Boussinesq terrain-following OGCM for oceanographic and geodetic applications. *Adv. Geosci.*, **18**, 63–86.

Trenberth, K. E., and J. T. Fasullo, 2009: Changes in the flow of energy through the Earth's climate system. *Meteor. Z.*, **18**, 369–377, doi:10.1127/0941-2948/2009/0388.

——, and ——, 2010: Tracking Earth's energy. *Science*, **328**, 316–317, doi:10.1126/science.1187272.

——, ——, and J. Kiehl, 2009: Earth's global energy budget. *Bull. Amer. Meteor. Soc.*, **90**, 311–324, doi:10.1175/2008BAMS2634.1.

von Schuckmann, K., J.-B. Sallée, D. Chambers, P.-Y. Le Traon, C. Cabanes, F. Gaillard, S. Speich, and M. Hamon, 2014: Consistency of the current global ocean observing systems from an Argo perspective. *Ocean Sci.*, **10**, 547–557, doi:10.5194/os-10-547-2014.

Wang, G., M. Dai, S. S. P. Shen, Y. Bai, and Y. Xu, 2014: Quantifying uncertainty sources in the gridded data of sea surface CO_2 partial pressure. *J. Geophys. Res. Oceans*, **119**, 5181–5189, doi:10.1002/2013JC009577.

Wunsch, C., and P. Heimbach, P., 2013: Dynamically and kinematically consistent global ocean circulation and ice state estimates. *Ocean Circulation and Climate: A 21st Century Perspective*, G. Siedler et al., Eds., International Geophysics Series, Vol. 103, Academic Press, 553–579.

Zhang, L., and T. Qu, 2015: Low-frequency variability of the South Pacific Subtropical Gyre as seen from satellite altimetry and Argo. *J. Phys. Oceanogr.*, **45**, 3083–3098, doi:10.1175/JPO-D-15-0026.1.

Brought to you by NOAA Central Library | Unauthenticated | Downloaded 01/16/24 07:32 PM UTC